Tectonics

RESEARCH ARTICLE
10.1029/2020TC006219

Key Points:
- The lithosphere is thick beneath the Himalaya while it is relatively thin beneath Tibetan plateau which mimics the variations in Moho depth and T_e
- The predominance of mantle isostasy beneath the northern Tibetan plateau predicts hot and deformable lithosphere
- Study reveals underthrusting of cold Indian mantle beneath the Himalayas

Supporting Information:
- Supporting Information S1

Correspondence to:
M. Ravikumar,
ravikumarmuppidi@gmail.com

Citation:
Ravikumar, M., Singh, B., Pavan Kumar, V., Satyakumar, A. V., Ramesh, D. S., & Tiwari, V. M. (2020). Lithospheric density structure and effective elastic thickness beneath Himalaya and Tibetan plateau: Inference from the integrated analysis of gravity, geoid, and topographic data incorporating seismic constraints. *Tectonics*, *39*, e2020TC006219. https://doi.org/10.1029/2020TC006219

Received 31 MAR 2020
Accepted 8 SEP 2020
Accepted article online 22 SEP 2020

Lithospheric Density Structure and Effective Elastic Thickness Beneath Himalaya and Tibetan Plateau: Inference From the Integrated Analysis of Gravity, Geoid, and Topographic Data Incorporating Seismic Constraints

M. Ravikumar[1], B. Singh[1,2], V. Pavan Kumar[1], A. V. Satyakumar[1], D. S. Ramesh[2], and V. M. Tiwari[1]

[1]CSIR-National Geophysical Research Institute (CSIR-NGRI), Hyderabad, India, [2]Indian Institute of Geomagnetism, Navi Mumbai, India

Abstract Investigation of deep crustal and lithospheric structures is essential to understand the nature of geodynamical processes beneath the Himalaya and Tibetan plateau of the India-Eurasia collision zone. Our density cross sections across the Himalaya-Eurasia collision zone using integrated 2-D modeling of gravity, topography, and geoid data incorporating constraints from seismic information supports the above contention. Analysis of gravity, geoid, and elevation data over the interior of the Tibetan plateau predicts complete isostatic compensation, whereas margins of the plateau, having large topographic gradients, show lack of isostatic compensation as the Airy Moho differs from flexural Moho and seismic Moho beneath the Himalaya. Our 2-D modeled lithospheric cross sections show thick crust (~75 km) and thick lithosphere (~240 km) beneath the Himalayas and southern Tibetan plateau and relatively thin crust (~60 km) and thin lithosphere (~140 km) beneath the northern Tibetan plateau. Therefore, depth of lithosphere-asthenosphere boundary (LAB) mimics the Moho relief. Thinner crust and thin lithosphere under northern Tibetan plateau suggest the importance of the mantle isostasy where the temperature is anomalously high. This corroborates with the presence of recent potassic volcanism, inefficient Sn propagation, east and southeast oriented global positioning system displacements, and large shear wave splitting anisotropy (>2 s). Excellent correlation between effective elastic thickness and lithospheric thickness predicts hot and deformable lithosphere in the northern Tibet and underthrusting of cold Indian mantle beneath the Himalayas.

1. Introduction

The collision of Indian plate with Eurasian plate is perhaps one of the most important tectonic events of the Cenozoic period, and it is responsible for the high elevation of the Himalaya and Tibetan plateau (Figure 1). Geodetic measurements suggest that the convergence between India and Eurasia is not only interplate but also intraplate within Tibetan plateau (Gan et al., 2007; Ge et al., 2015). Convergence estimates based on paleomagnetic data indicate that it varies along the Himalayan arc, increasing from 1,800 km in the western sector to 2,475 km in the central and reaching 2,800 km in the east (Johnson, 2002). This deformation pattern represents N-S compression and E-W extension of Tibetan plateau. It is widely speculated that lithospheric mantle processes accommodate the total convergence (Chen et al., 2017). Since the entire lithosphere is involved in the deformation, the study of the crust and lithosphere of the tectonically active area is significant to understand continental rheology and its evolution. It is well known that underthrusting of the Indian lithospheric plate plays a substantial role in the growth of the Himalaya and Tibetan plateau (Yin & Harrison, 2000). However, there are conflicting views regarding the extent of underthrusting of the Indian lithosphere beneath the Himalaya and Tibetan plateau (Chen et al., 2017; Li & Song, 2018; Zhao et al., 2010).

Physical properties and configuration of the Indian and Eurasian lithosphere beneath the Himalaya-Tibet collision zone are debated in light of contrasting yet competing models such as (i) thrusting of the Indian mantle lithosphere under Tibet (Owens & Zandt, 1997; Zhou & Murphy, 2005), (ii) low angle (Owens & Zandt, 1997) and high angle (Li et al., 2008; Liang et al., 2012; Tilmann et al., 2003) subduction of the Indian lithosphere beneath Tibetan plateau, and southward-northward subduction (Kind & Yuan, 2010;

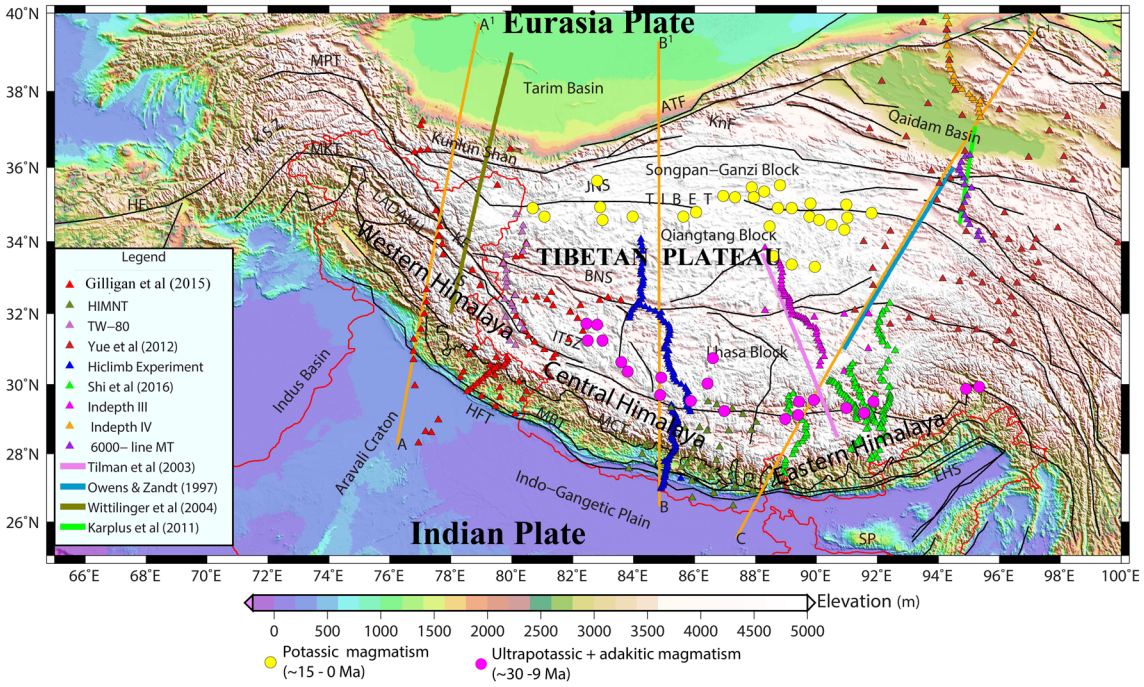

Figure 1. Topographic map of Himalaya, Tibetan plateau and surrounding regions (SRTM-30′ data) with important tectonic elements of Tibet adopted from Yin and Harrison (2000) and Taylor and Yin (2009). Indus-Tsangpo Suture Zone (ITSZ) separates Himalaya towards the south and Lhasa block of Tibet towards the north. Himalayan Frontal Thrust (MFT), Main Boundary Thrust (MBT) and Main Central Thrust (MCT) are important units of Himalaya with Ganga basin (GB) south of it representing a foreland basin. Bangong-Nujiang Suture (BNS), Jinsa Nujiang Suture (JNS); Kunlun Fault (KnF) and Altyn Tagh Fault (ATF) represent important units of Tibet. MKT, Main Karakoram Thrust; IS, Indus suture; MPT, Main Pamir Thrust; HKSZ, Hindu Kush Seismic Zone; KF, Karakoram Fault; CF, Chamman Fault; HF, Herat Fault. This figure also shows various seismic and MT experiments (see index map) for constraining our gravity models. The profiles A-A′, B-B′, and C-C′ are modeled for the 2-D density structure for the present study. Yellow and black filled circles mark two different episodes of magmatism distributions (Chung et al., 2005, 2009).

Zhao et al., 2010, 2011), (iii) crustal shortening and thickening by pure shear (Murphy et al., 1997), and (iv) delamination or convective removal of tectonically thickened lithospheric mantle (Chen et al., 2017; England & Houseman, 1989; Jiménez-Munt & Platt, 2006; Molnar et al., 1993).

Reliable information on crust and lithospheric structure beneath the Tibetan plateau has been obtained through various seismic experiments such as Sino-American PASSCAL broadband (McNamara et al., 1997; Owens & Zandt, 1997), Hi-CLIMB (Himalayan-Tibetan Continental Lithosphere during Mountain Building) experiments (Nabelek et al., 2009), TW-80 (Zhang et al., 2014), and the international and multidisciplinary IN-DEPTH experiments (Brown et al., 1996; Hauck et al., 1998; Karplus et al., 2011; Kind et al., 2002; Nelson et al., 1996; Unsworth et al., 2005; Zhao et al., 1993, 2001). The series of Sino-French seismic studies (Hirn et al., 1995; Jiang et al., 2006; Schulte-Pelkum et al., 2005), ANTILOPE (Zhao et al., 2010), and Gangdese network (Shi et al., 2015, 2016) also provided valuable information on lithospheric structure and geodynamic process (Figure 1).

Seismic tomographic and receiver function studies can map the geometry and northern extent of Indian mantle lithosphere beneath the Himalaya and Tibetan plateau based on high-velocity anomalies and shed light on Tibetan tectonic evolution (Agius & Lebedev, 2013; Barazangi & Ni, 1982; Chen et al., 2017; Kumar et al., 2005, 2006; Lebedev & van der Hilst, 2008; Li et al., 2008; McNamara et al., 1997; Priestley et al., 2006; Ramesh et al., 2005; Replumaz et al., 2010; Shapiro & Ritzwoller, 2002; Shi et al., 2015, 2016; Zhao et al., 2010, 2011). The high-velocity mantle lithosphere beneath the Himalayas and southernmost Tibetan plateau is most likely the underthrusting Indian lithosphere (Priestley et al., 2006; Tilmann et al., 2003). However, differences among existing seismic images complicate the interpretation of mantle lithospheric process (Chen et al., 2017). For example, the lithospheric mantle configuration beneath the central, northern, and eastern Himalaya-Tibet zone in terms of geometry, northern extent, and convergence angle of Indian lithosphere remains contentious (e.g., Kosarev et al., 1999; Li et al., 2008; Nabelek et al., 2009; Tilmann et al., 2003; Zhao et al., 2010).

Gravimetric studies of Himalayas and Tibetan plateau based on Airy isostasy and spectral analysis methods have mainly brought out large scale Moho undulations using ground gravity (Braitenberg et al., 2000, 2003; He et al., 2014; Jin et al., 1994, 1996) and satellite-derived GRACE and GOCE data (Bagherbandi, 2011; Basuyau et al., 2013; McKenzie et al., 2019; Shin et al., 2007; Tenzer et al., 2015; Zhao et al., 2020). Studies based on the flexural modeling approach (Braitenberg et al., 2003; Cattin et al., 2001; Chen et al., 2015; Hetényi et al., 2006; Tiwari et al., 2006, 2008) have yielded lower values of effective elastic thickness (<40 km) over Tibetan plateau and higher values (>50 km) over the adjoining Indian shield suggesting thin and thick lithosphere, respectively. Recent studies based on integrated modeling of gravity, geoid, topography, and heat flow data incorporating seismic and petrological constraints along selected profiles in western, central, and eastern region of Himalaya and Tibetan plateau have revealed significant reduction in lithospheric thickness beneath the northern Tibet and increase in lithospheric thickness below the Himalayas and southern Tibet (e.g., Afonso et al., 2019; Jiménez-Munt et al., 2008; Tunini et al., 2016). However, uncertainties remain on the nature of lithosphere beneath the northern Tibetan plateau as well as on the extension and geometry of underthrusting Indian lithospheric plate beneath the India-Eurasia collision zone.

The India-Eurasia continental collision has produced Cenozoic volcanic rocks on the Tibetan plateau which show systematic compositional variations in space and time. Xia et al. (2011) attributed these systematic variations in volcanism to various geodynamic processes that include convective removal of the thickened lithospheric root followed by asthenospheric upwelling (Molnar et al., 1993).

In this study, we present an overview of the current scientific knowledge of the Himalaya and Tibetan plateau based on geopotential models with constraints from seismic and seismological information. Our 2-D lithospheric density cross sections derived from integrated modeling of gravity, topography, geoid data, and integration with estimates of effective elastic thickness and state of isostasy offer new insights into linkages between lithospheric evolution and surface expressions of Tibetan plateau uplift and volcanism. The poor correlation between the high topography and crustal thickness renders application of local compensation models (e.g., Airy-Heiskanen or Pratt-Hayford) problematic (Tseng et al., 2009). Thus, understanding the mechanism of isostatic compensation of topography of the Himalaya and Tibetan plateau could provide constraints on the relative role of sublithospheric buoyancy versus lithospheric support. Our study revealed predominance of mantle isostasy in the northern Tibetan plateau due to thinning of the lithosphere that helped to demarcate the northern extent of the Indian lithospheric mantle (ILM) along three selected profiles (Figure 1) in the western (A-A′), central (B-B′), and eastern (C-C′) part of India-Eurasia collision zone.

2. Geotectonic Background

The India-Eurasia collision zone consists of the accreted domain of crustal and lithospheric components. The Indian peninsula (the Precambrian Indian shield) represents a collage of cratonic blocks and mobile belts assembled between mid-Archean and neo-Proterozoic times. The Himalaya-Orogen (Figure 1) is divided into three major east-west tectonic units: the lesser Himalaya, the higher Himalaya, and Tethys Himalaya. These units are separated from each other by major crustal scale thrusts, named, from south to north: (1) Himalayan Frontal Thrust (HFT), formed at about 4–2 Ma along which Siwalik sediments of Plio-Quaternary times are emplaced over the recent sediments/alluvium of Ganga basin; (2) Main Boundary Thrust (MBT), formed at about 12 Ma along which the Paleozoic and the Proterozoic metasediments are thrusted over the Plio-Quaternary Siwalik sediments to form Lesser Himalaya; (3) Main Central Thrust (MCT) formed at about 20 Ma along the northern margin of the Indian plate when the crystalline rocks of Higher Himalaya are thrusted over the Paleozoic and the Proterozoic metasediments (Mishra et al., 2012; Yin & Harrison, 2000) (Figure 1). Further north, the Indus-Tsangpo Suture Zone (ITSZ) represents the suture zone between India and Eurasia plate that includes ophiolites, deep sea sediments deposited on the Neo-Tethys ocean floor and Mesozoic island-arc volcanic rocks (Yin & Harrison, 2000). To the west of 78°E longitude, ITS zone splits into Ladakh and Karakorum ranges which represent the westward prolongation of the Lhasa and Qiangtang terrain, respectively. The western sector shows complex tectonics due to the occurrence of Kohistan arc in between the Indian and the Eurasia plates forming two sutures, namely, Main Mantle Thrust (MMT) which is the westward extension of ITSZ and Main Karakoram Thrust (MKT) or northern suture where Indian plate subducts northward.

The Tibetan plateau consists of an agglomeration of several east-west trending terrains that were successively accreted to the southern margin of the Eurasian plate during late Paleozoic and Mesozoic time (Allegre et al., 1984; Dewey et al., 1988). These terrains include (1) Lhasa terrain in the south, (2) Qiangtang terrain in the center, and (3) Songpan-Ganzi terrain in the north. Lhasa terrain is bounded by BNS (Bangong-Nujiang suture) toward the north and Indus Tsangpo Suture Zone (ITSZ) in the south (Figure 1). It primarily consists of paragneisses and granitic gneisses as a basement. The cover rock is Ordovician to Carboniferous carbonate and clastic rocks (Yin & Harrison, 2000). Qiangtang terrain is bounded by Bangong-Nujiang Suture (BNS) toward the south and Jinsha River Suture (JRS) toward the north (Figure 1). The basement rocks are gneisses and metavolcanics over the plateau, while the basin toward the east consists of Ordovician and Silurian unmetamorphosed or slightly metamorphosed sediments which rest on the crystalline basement. BNS is characterized by the presence of ophiolite rocks which may represent an earlier subduction zone similar to ITSZ (Allegre et al., 1984). Songpon Ganzi terrain represents a trench-arc-basin system of a convergent margin that is mostly covered by tertiary deposits. The island arc comprises andesite with a lesser amount of basalt (Yin & Harrison, 2000). The Tarim basin, which is the largest cratonic domain toward the north of ATF (Figure 1), is covered by 4 to 12 km of thick sediments belonging to Ordovician, Permian, and Cretaceous periods (Gao & Ye, 1997).

Cenozoic volcanic rocks produced as the result of India-Eurasia continental collision are widespread on Tibetan plateau and show systematic compositional variations in space and time. The sodium and potassium-rich lavas of 65 to 40 Ma are present mainly in the Lhasa terrane, whereas Qiangtang terrane shows the widespread distribution of potassic-ultrapotassic lavas and subordinate adakites of ~45 to 26 Ma. The post-collisional volcanism produced ultrapotassic and adakitic lavas coevally between ~26 and 8 Ma in the Lhasa terrane, and potassic and minor adakitic volcanism became extensive since ~20 Ma in the western Qiangtang and Songpan-Ganzi terranes (Figure 1). Xia et al. (2011) interpreted these systematic variations in volcanism due to various geodynamic processes that evolved at depth to form the Tibetan plateau. These processes include convective removal of the thickened lithospheric root followed by asthenospheric upwelling as proposed by Molnar et al. (1993).

3. Data and Methodology

3.1. Data

The elevation data used in the present study (Figure 1) are taken from the Shuttle Radar Topography Mission (SRTM) having 30 m (1-arc-second) resolution (http://topex.ucsd.edu/cgi-bin/get_srtm30.cgil). The most striking feature of the map is a relatively flat but hefty topography of the Tibetan plateau with steep gradients at the margins. The topography of the western Tibetan plateau is somewhat higher (5,000 m) compared to eastern Tibetan plateau (4,500 m) and is significantly narrower (400 km) than the eastern Tibet (1,000 km). Despite the uniform elevation of the Tibetan plateau, inferred density structure of the crust and lithosphere is quite different from southern Tibetan plateau to northern Tibetan plateau (Jiménez-Munt et al., 2008; Tunini et al., 2016).

The Bouguer anomaly map (Figure 2), which is the final product of gravity observations, has been prepared after applying the complete Bouguer correction to free-air anomaly data derived from the GGM05C global earth model (Ries et al., 2016, http://doi.org/10.5880/icgem.2016.002) using FA2BOU software (Fullea et al., 2008) with reduction density of 2.67 g/cm^3. The GGM05C global gravity model was estimated to spherical harmonic of degree and order 360 from a combination of GRACE and GOCE gravity information and surface gravity anomalies from DTU13 (Andersen et al., 2014). The most predominant feature of the Bouguer anomaly map is a long wavelength gravity low encompassing the entire Tibetan plateau (L1, ~−500 mGal) that is attributed mainly to crustal thickening due to isostasy (Jin et al., 1996). This gravity low is flanked by steep gradients related to Himalayan thrusts and suture zones toward the south and Kunlun and Altyn Tagh faults toward the north, respectively, whereas Ganga basin (H1), Indus basin (H2), and Tarim basin (H3) show relatively positive gravity anomaly (−50 mGal) due to crustal bulge related to lithospheric flexure (Ravikumar, Mishra, & Singh, 2013; Ravikumar, Mishra, Singh, Venkat Raju, et al., 2013; Turcotte & Schubert, 2001). Since orogenic belts are characterized by long wavelength Bouguer gravity anomalies due to isostatic compensation, the small wavelength features due to shallow sources are not well recognized in this map.

10.1029/2020TC006219

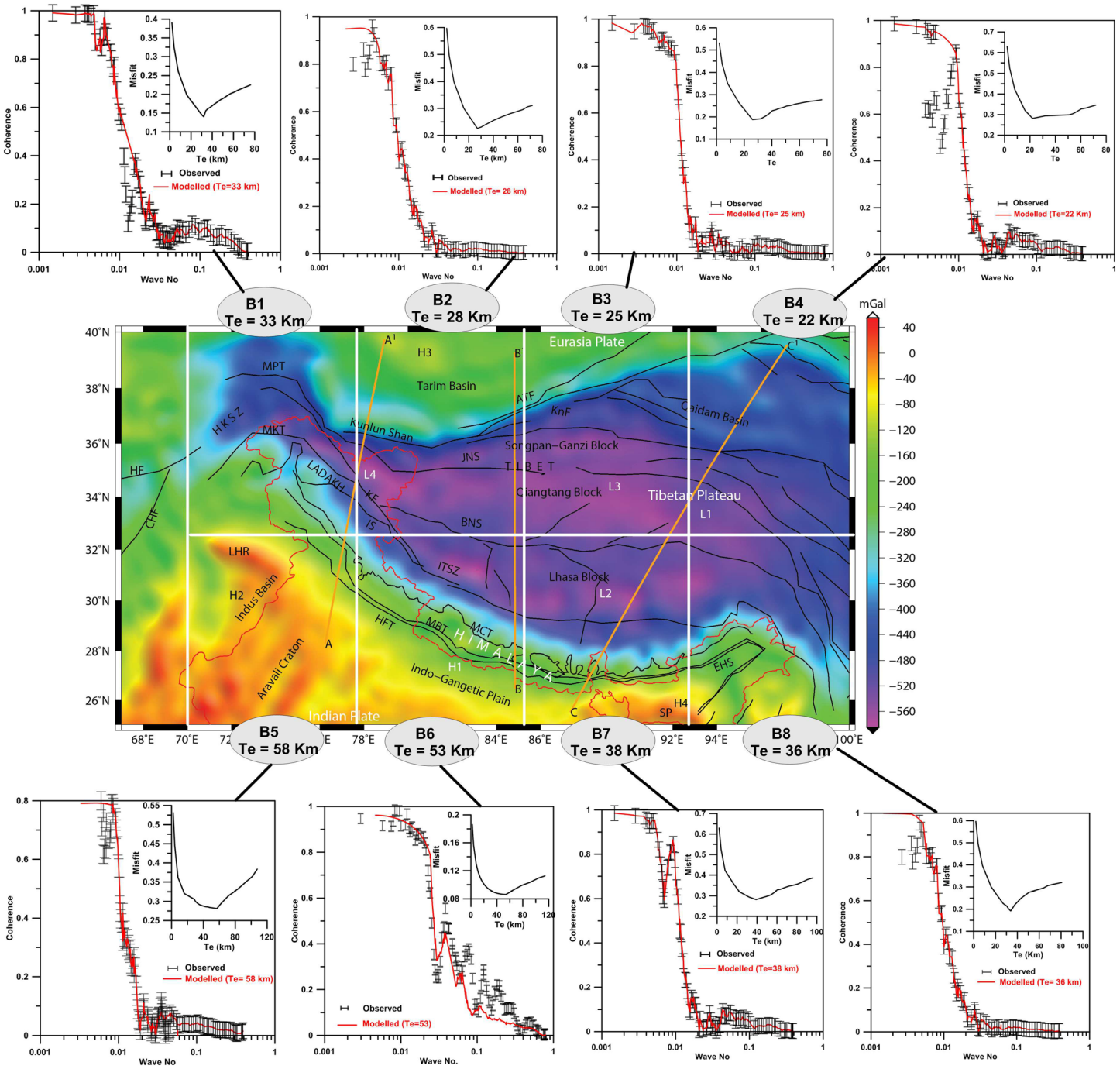

Figure 2. Complete Bouguer anomaly map of Himalaya and Tibetan plateau obtained from satellite free-air anomaly data (Ries et al., 2016; http://doi.org/10.5880/icgem.2016.002) using SRTM-30′ data (Figure 1). It shows the smallest (<−550 mGal) long wavelength gravity lows (L1, L2, L3, and L4) over Tibetan plateau related to deep-seated mass deficiency caused due to isostatic compensation. The gravity highs are related to Himalayan Thrusts (H1), Indus basin (H2), Tarim basin (H3), and Shillong plateau (H4), respectively. This figure also shows effective elastic thickness (T_e) of Himalaya-Tibetan plateau based on coherence between Bouguer anomaly and topography using maximum entropy method (Forsyth, 1985; Lowry & Smith, 1994). T_e values are invariably high (~58 km) over the Indian shield region whereas T_e values are generally low (<30 km) over the northern Tibetan plateau such as over the Qiangtang (Block B3) and northeastern Tibetan plateau (Block B4) (see text for details in section 4.2).

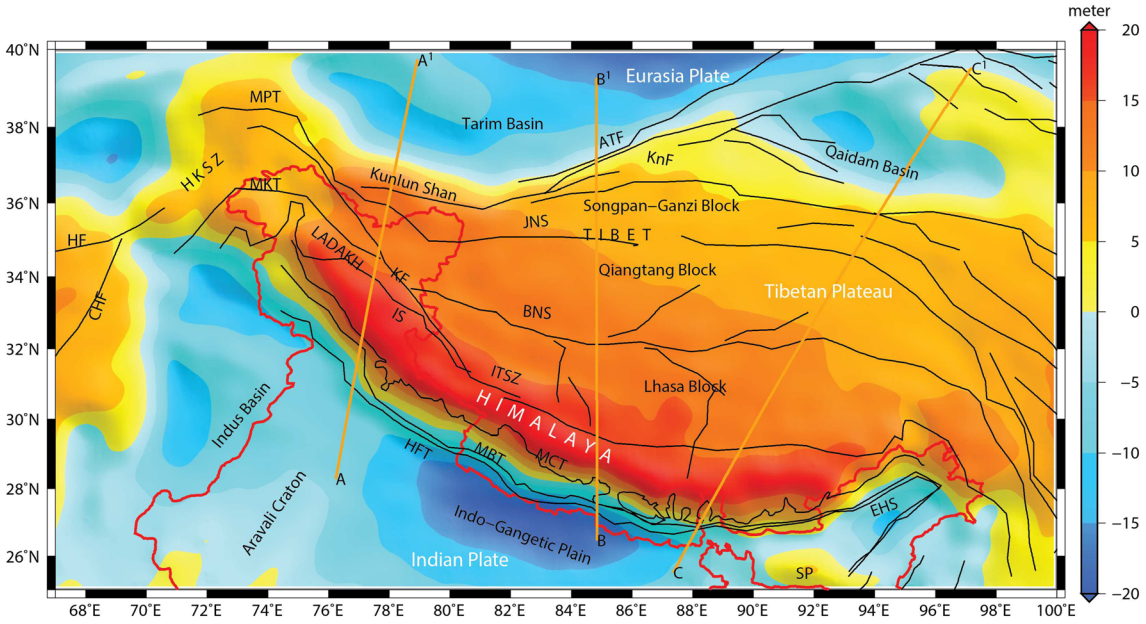

Figure 3. The map shows geoid undulations from EGM-2008 model filtered to degree and order 11 (Afonso et al., 2019; Bowin, 1983; Robert et al., 2015). It depicts gradient at the Himalayan front and the northern margin of the Tibetan plateau. The values over the Himalaya vary between 15 and 20 m and gradually decrease to 5 m toward the NE part of the plateau and are associated with the deep lithospheric density distribution.

The Bouguer anomaly map over the Tibetan plateau also shows two distinct linear gravity lows: one in the southern part of the Lhasa (L2, ~−450 mGal) associated with the crustal thickening and one in the northern part of Qiangtang region (L3, ~−550 mGal) allied with the extensive distribution of Cenozoic volcanic rocks of mantle origin (Deng et al., 1996; He et al., 2010). He et al. (2014) postulated that the reduction in density occurred in the lower crust and lithosphere mantle due to the extensive eruption of ultra-potassic volcanoes in the northern Tibetan plateau. Another prominent gravity anomaly low (L4) observed over the western part of the Qiangtang region is attributed to the presence of large crustal thickness (Rai et al., 2006; Wittlinger et al., 2004). The Lahore Sargodha Ridge (LHR) is reflected as a prominent gravity high in NW India. In northeast India, Shilling plateau with a topographic rise of ~2.0 km is associated with positive Bouguer (H4) and positive free-air gravity anomalies pointing lack of isostatic compensation. There are other significant short wavelength anomalies present in the Bouguer anomaly map (Figure 2) caused due to shallow crustal sources. However, owing to the regional nature of the present study these are not discussed here.

Figure 3 shows the geoidal undulations extracted from the EGM2008 global model (Pavlis et al., 2012). The EGM2008 gravitational model is complete to spherical harmonic degree and order 2159. Several theoretical and empirical studies suggest that under some reasonable assumptions, removing spherical harmonics lower than 8 to 15 from the total geoid results in a signal controlled mostly by density anomalies within the first 300 to 410 km (e.g., Afonso et al., 2019; Bowin, 2000; Coblentz et al., 2011). In the present study, in order to avoid the effects of sublithospheric density variations, the geoid anomaly was filtered to remove the signature corresponding to the lower spherical harmonics until degree and order 11 (Afonso et al., 2019; Bowin, 1983; Robert et al., 2015). The most significant feature of the geoid undulation map is the presence of large amplitude positive geoid high (~15 to 20 m) along the Himalayan arc which gradually decreases to ~5 m over the northern part of the Tibetan plateau probably caused due to thinning of the lithosphere. Basins are characterized by geoidal lows displaying minimum values as observed over the Ganga basin (−20 m), Tarim basin (−10 m), and Qaidam basin (−8 m).

3.2. Methodology

3.2.1. The Airy and Flexural Isostasy

The use of isostatic analysis in delineating the deep-seated structures is well established. The derived regional isostatic anomaly is independent of the measured gravity field and reflects more closely the deep structure of the region. In large mountainous regions, near zero, positive free-air anomaly is proxy to state of

complete isostasy (Watts, 2001). Both free-air gravity and topography show that the Tibetan plateau is everywhere isostatically compensated at wavelength greater than 100 km (McKenzie et al., 2019). Jin et al. (1994) studied statistical and spectral properties of the gravity and topography data of Tibetan plateau. Their results show positive correlation at wavelengths <150 km and negative correlation >250 km. Considering various isostatic studies over diverse regions (Bagherbandi, 2011; Braitenberg et al., 2000; Jordan & Watts, 2005; Shin et al., 2007), it is found that isostasy is a regional phenomenon and manifests over a region having large topographic load of wavelength greater than 250 km. Therefore, a regional topography map using a low pass filter with a cutoff wavelength of 250 km is used to compute the Airy (1855) crustal root assuming a density contrast of −0.40 g/cm^3 (Simpson et al., 1986) between the crust and mantle interface with a reference crustal thickness of 40 km. The crustal thickness in the southern end of the profiles is reported to be ~40 km. Therefore, the reference depth of ~40 km is chosen in the present study and is similar to previous studies in this region (Jiménez-Munt et al., 2008; Singh et al., 2017; Tiwari et al., 2013; Tunini et al., 2016).

The presence of significant negative Bouguer anomalies (Figure 2) associated with long wavelength regional topography of Tibetan plateau reveals the state of near complete isostatic compensation over the region (e.g., Braitenberg et al., 2000; Jiménez-Munt et al., 2008; Shin et al., 2007). However, the Himalayas show deviations from Airy isostasy (e.g., Cattin et al., 2001; Lyon-Caen & Molnar, 1983; Tiwari et al., 2006). Therefore, the interior of the Tibetan plateau is isostatically compensated except at the margins which show a large topographic gradient due to flexural effects (McKenzie et al., 2019). Assuming that isostatic compensation takes place at Moho, we have obtained Moho undulations based on local isostatic compensation (Figure S1; Airy, 1855) and regional isostatic compensation (Figure S2, flexural models; Vening Meinesz, 1931) of the Himalaya-Tibetan plateau (see supporting information for details). To compute flexural Moho, we first calculated effective elastic thickness (T_e) using maximum entropy method (MEM) (Lowry & Smith, 1994), which provides a measure of the degree of flexural compensation in response to long-term tectonic loads (Audet et al., 2007; Watts, 2001). Our basic assumptions while estimating the effective elastic thickness (T_e) from coherence analysis are that long wavelength topography is isostatically compensated, mean topography and Bouguer gravity anomaly are coherent, and short wavelength topography is uncompensated, that is, Bouguer anomaly is incoherent with topography (Forsyth, 1985). We divided the study area (longitude: 70°E–100°E, latitude: 25°N–40°N) into eight (8) equal blocks and computed T_e for each block, and the results are shown in Figure 2. The parameters used for calculating T_e are (i) Young's modulus $E = 10^{11}$ Pa and (ii) Poisson's ratio $v = 0.25$ with reference depth 40 km. And finally, we computed flexural Moho (Figure S2) based on the methodology followed by Vening Meinesz (1931). Vening Meinesz assumed that the lithosphere is an elastic shell with the thickness T_e, which can be determined according to the coherence methods discussed above (Forsyth, 1985; Lowry & Smith, 1994) comparing gravity data to topographic heights. The flexural Moho calculated for different T_e values (20, 30, 40, and 50 km, Figure S2) using mechanical parameters of the lithosphere: flexural rigidity (D), Young's modulus ($E = 10^{11}$ Pa), and Poisson's ratio ($v = 0.25$). The T_e of 40 km model fits well with observations (Gravity and seismic Moho models) and is plotted along with the model profiles. Also, the T_e estimates, determined from coherence between the topography and Bouguer gravity anomalies, over the eight rectangular blocks average to ~40 km, which is in the similar range of T_e value reported by other studies (Braitenberg et al., 2003).

3.2.2. Modeling Strategy

It is well known that modeling of gravity field alone is not unique. To arrive at a plausible density model, geoid undulations and topography are also modeled along with gravity fields. The combined use of gravity, elevation, and geoid undulations will be useful in separating out mass inhomogeneities occurring within the mantle from those confined to the crust. This becomes possible because the effect on gravity due to given density variation decays with the square of the distance and therefore decreases rapidly with depth. On the other hand, the depth dependence of geoid anomalies is proportional to the inverse of distance, which makes geoid anomalies comparatively more sensitive to deep seated lithospheric heterogeneities (Turcotte & Schubert, 1982). The crustal and lithospheric thickness and its density distribution affect the gravity anomalies, geoid undulations, and topography. Thus, the values of gravity anomaly and geoid undulations are dependent on distance to the source, whereas elevation is independent of distance; all are effective on different depth ranges (Zeyen & Fernàndez, 1994). The Bouguer anomalies are more sensitive to crustal density distribution, whereas elevation is very sensitive to changes in density and thickness of the lithospheric mantle (Zeyen & Fernàndez, 1994).

Gravity anomalies are calculated using GM-SYS professional software (GM-SYS, 2000) which is based on Talwani's 2-D algorithm (Talwani et al., 1959), while geoid and topography undulations are calculated using 2-D Litmod-2.0 forward modeling algorithm (Afonso et al., 2008; Kumar et al., 2019). LitMod-2D_2.0 is a numerical code, which combines geophysical and petrological data to infer the crustal and upper mantle structure down to 410 km depth (Afonso et al., 2008; Kumar et al., 2019). The code calculates the 2-D distribution of temperature, density, and mantle seismic velocities and the resulting surface heat flow, elevation, gravity, and geoid anomalies (Afonso et al., 2008; Kumar et al., 2019). LitMod-2D_2.0 works under a forward modeling scheme; at each step, the model outputs (elevation, gravity and geoid anomalies, surface heat flow, and mantle seismic velocities) are compared with observed data (geophysical observables, seismic velocities, and tomography images), and the input parameters and model geometry can be modified by the user within the experimental uncertainties, in a trial and error procedure until the best fitting model is obtained (see Kumar et al., 2019; Tunini et al., 2016, for further details). In the present study, we begin from the bottom of the section and adopt the following steps to arrive at a final density model.

1. Firstly, the initial geometry of the LAB is obtained from various seismological experiments (Acton et al., 2010; Agius & Lebedev, 2013; Chen et al., 2017; Li et al., 2008; Li & Song, 2018; Nabelek et al., 2009; Priestley et al., 2008; Shi et al., 2015, 2016; Zhao et al., 2010, and references therein), while depth of Moho is obtained from seismic and seismological results (Figure S3). Since lithospheric mantle density depends on temperature and composition, first, we introduced the temperature dependent heterogeneity in the lithospheric mantle density (ρ_m) according to $\rho_m = \rho_a\,(1 + \alpha\,(Ta - T(z))$, where ρ_a is the density of the asthenosphere (3.20 g/cm^3) considered constant everywhere, α is the thermal expansion coefficient, Ta is the temperature at the LAB and is 1350°C, and T(z) is the temperature of the lithospheric mantle at a given depth z (Zeyen & Fernàndez, 1994) and T(z) is adopted from Jiménez-Munt et al. (2008). In order to incorporate temperature-dependent density variations in GM-SYS modeling algorithm which require layers of discrete densities, the lithospheric mantle is divided into three layers starting from LAB to Moho with (a) average density of 3.22 g/cm^3 corresponding to temperature ranging from 1350°C to 1200°C, (b) average density of 3.239 g/cm^3 for temperature ranging from 1200°C to 1000°C, (c) and average density of 3.28 g/cm^3 for temperature ranging from 1000°C to 800°C. Gravity response of this initial density model is compared with the long wavelength regional gravity anomaly (LWRGA) derived from the observed Bouguer gravity anomaly. Based on spectral analysis approach, we derived LWRGA, using a low pass filter with a cutoff wavelength >300 km (Jin et al., 1996; Shin et al., 2007). This contains signal due to undulations from Moho interface as well as subcrustal lithospheric sources (Figure S4: image). Previous studies also reported that the source of the Bouguer gravity anomaly at wavelengths greater than 230 to 300 km is located at the presumed depth of the Moho or even deeper (e.g., Braitenberg et al., 2003; Jin et al., 1996; Shin et al., 2007; Tiwari et al., 2013). To justify this wavelength, we derived isostatic regional Bouguer anomaly (IRBA) corresponding to near zero free-air anomaly values (Subba Rao, 1996). IRBA represents unbiased estimate of deficit of mass in the subsurface due to compensated topography irrespective of mode and level of compensation. To make our point more clear, we superimposed IRBA anomaly contours (Figure S4: contours) over low pass filtered long wavelength gravity anomaly image map (wavelength >300 km, low pass filter, Figure S4: image), and they appear quite similar in amplitude and outline (see Figure S4 for details). Further, to make the model more robust, we also model the geoidal undulations and topography as an additional constraint to resolve lithospheric thickness. The geoid calculations are carried out using a simple algorithm applied to the element of the mesh, and elevation is calculated at each column of the mesh under the assumption of local isostasy (Zeyen et al., 2005, for further details). The geometry of the LAB and Moho are modified until the best fit is obtained.
2. Secondly, since the lithospheric density also depends on pressure and composition, we adopted LitMod-2D_2.0 approach as adopted by Tunini et al. (2016) and Afonso et al. (2019). In the present simulation, mantle mineral compositions with weight percent of SiO2 - 45.50; Al_2O_3 - 3.80; FeO - 8.50; MgO - 39.80; CaO - 3.50; Na_2O - 0.25 have been used which represents the average chemical composition of the lithospheric mantle. The mineral assemblages (NCFMAS) were measured by the external module GENERATOR using a Gibbs free-energy minimization algorithm (Connolly, 2005) for pressure and temperature ranges in lithospheric mantle. All the stable assemblages in this study were computed using modified version of thermodynamic database (Afonso & Zlotnik, 2011; Holland & Powell, 1998). The detailed methodology and workflow of the Litmod-2D_2.0 can be found in Kumar et al. (2020). The

geometry of the LAB and Moho are modified until the best fit is observed. We access the two different density models for our study, according to Zeyen and Fernàndez (1994), a decrease in density from the lithospheric mantle with increasing temperature using the asthenospheric density as a reference. Whereas if we include material property (mineral composition) of the mantle based on LitMod approach (Afonso et al., 2008), the density continuously increases from lithospheric mantle to the sublithospheric mantle due to predominant effect of pressure (Afonso et al., 2019; Tunini et al., 2016). It is interesting to observe that despite large differences in the density depth distribution obtained from thermal and petrological based simulations, the corresponding lithospheric model shows similar lithospheric geometry (see Figures S5 to S7).

3. Finally, we introduced the crustal density sources, primarily known from published geological and geophysical cross sections to the modeled section to match the short wavelength residual anomalies. Densities of the various bodies modeled in the sections are given in Table 1.

4. Results

The calculated Airy crustal root and flexural Moho ($T_e = 40$ km) are also shown in the modeled section along the selected profiles (Figures 4–6: panel c). As expected, beneath the Himalaya, the Airy Moho departs from flexural Moho and appears to be under compensated (Cattin et al., 2001; Tiwari et al., 2006). Therefore, flexural model has been used widely in Himalaya (Cattin et al., 2001; Hetényi et al., 2006; Lyon-Caen & Molnar, 1983; Tiwari et al., 2006). We also observe significant mismatch between Airy, flexural, and modeled gravity Moho based on seismic constraints, especially over the northern part of the Tibetan plateau (Figure S3). Thinner crust and thin lithosphere under northern Lhasa and Qiangtang terrain where the temperature is also anomalously high, the role of mantle isostasy appear to justify the offset (Jiménez-Munt et al., 2008; Tseng et al., 2009). Tseng et al. (2009) speculated the linkage of offset in Moho in the central and northern part of Tibetan plateau to flexural strength of the lithospheric mantle. Low T_e values over northern Tibetan plateau indicate that the lithosphere is weak in this region (Figure 2, T_e Blocks 3 and 4). The effective elastic thickness (T_e) results are described in detail in section 4.2. The best-fitting crustal and lithospheric density models are described in the following sections.

4.1. 2-D Lithospheric Structures Based on Gravity and Geoid Modeling

In the past, a variety of geophysical methods have been used to study the crust and lithospheric structure of the Himalaya and Tibet regions (Figure 1). Important among them are deep seismic studies (Galve et al., 2006; Haines et al., 2003), seismic tomography (Acton et al., 2010; Chen et al., 2017; Li et al., 2008; Li & Song, 2018; McNamara et al., 1997; Priestley et al., 2008), magnetotellurics (Unsworth et al., 2005; Wei et al., 2001), gravimetric studies (Braitenberg et al., 2000; Cattin et al., 2001; Hetényi et al., 2006, 2016; Jiang et al., 2004; Jiménez-Munt et al., 2008; Jin et al., 1994, 1996; McKenzie et al., 2019; Ravikumar, Mishra, & Singh, 2013; Ravikumar, Mishra, Singh, Venkat Raju, et al., 2013; Robert et al., 2015; Shin et al., 2007; Tiwari et al., 2006, 2008; Tunini et al., 2016; Zhao et al., 2020), receiver function studies (Gilligan et al., 2015; Mitra et al., 2005; Nabelek et al., 2009; Priestley et al., 2019; Rai et al., 2006; Shi et al., 2015, 2016; Wittlinger et al., 2004; Zhao et al., 2010), and geothermics (Chung et al., 2005), which provided useful constraints in building the initial model. For constraining the shallow crustal structure, geological cross-sections were adopted from Yin and Harrison (2000), Guillot et al. (2003), Wittlinger et al. (2004), and Searle (2010). Locations of profiles were primarily selected on the basis of the availability of seismic constraints at least over a part of the area (Figure S3).

We have considered average mantle composition for the entire mantle lithosphere due to the fact that the effect of temperature is dominant on lateral density variation rather than pressure and composition. Interestingly, studies have also indicated that despite large differences in density depth distribution obtained from thermal and geophysical-petrological approaches, the corresponding lithospheric models show similar lithospheric geometry (Tunini et al., 2015).

4.1.1. Crust and Lithospheric Mantle Structure Beneath the Western Part of Himalaya and Tibetan Plateau

The density structure of the lithosphere is less understood in the western part of Himalaya and Tibetan plateau due to the rugged and inaccessible nature of these terrains. Seismic constraints include Moho depths varying from ~40 km beneath the Indo-Gangetic plains to ~80 km beneath the Karakorum and Kunlun

Tectonics

10.1029/2020TC006219

Table 1
Physical Properties of the Different Tectonic Units Used in the Crustal Model Along A-A′, B-B′, and C-C′ Profiles

Tectonic units	Lithology	Density (ρ, g/cm^3)	Reference
1. Foreland basin	Alluvium sediments	2.4 (2.2–2.4)	Mishra et al. (2012); Ravikumar, Mishra, and Singh (2013), Ravikumar, Mishra, Singh, Venkat Raju, et al. (2013)
2. HFT	Siwalik sediments	2.5–2.55	Yin and Harrison (2000)
3. MBT	Paleozoic and the Proterozoic metasediments	2.65	Yin and Harrison (2000)
4. MCT	Crystalline rocks	2.74	Yin and Harrison (2000)
5. Tethys Himalaya	Ophiolities, deep sea sediments, Mesozoic island-arc and volcanic rocks	2.65	Yin and Harrison (2000); Jiménez-Munt et al. (2008); Bai et al. (2013)
6. Indian upper crust		2.7	Jiménez-Munt et al. (2008) and Bai et al. (2013)
7. Indian middle crust		2.9 (2.91–2.99)	Bai et al. (2013); Tunini et al. (2016)
8. Indian lower crust		3.0 (3.0–3.18)	Cattin et al. (2001); Tiwari et al. (2006); Hetényi et al. (2007); Bai et al. (2013); Tunini et al. (2016)
9. Eclogized crust (ELC)		3.1 (3.0–3.2)	Tiwari et al. (2006); Hetényi et al. (2007); Nabelek et al. (2009); Shi et al. (2015, 2016)
10. Ladakh batholiths	Green schist that grades to basalt and sheared granitoid	2.77 (2.72–2.8)	Searle (2010); Tunini et al. (2016)
11. West-Quingtang block	Low to high grade metamorphed melange complexes	2.76	Jiménez-Munt et al. (2008); Bai et al. (2013); Tunini et al. (2016)
12. Kunlun shan	Triassic complex sediments	2.72 (2.62–3.0)	Tunini et al. (2016)
13. Eurasia midcrust	Granitoid	2.8	Tunini et al. (2016); Searle (2010)
14. Tarim basin		2.45	Jiménez-Munt et al. (2008); Mishra et al. (2012); Tunini et al. (2016)
15. Eurasia upper crust		2.7	Jiménez-Munt et al. (2008); Bai et al. (2013); Tunini et al. (2016)
16. Eurasia lower crust		2.9–3.1	Zhang et al. (2014)
17. Gangdese batholith	Cretaceous-Tertiary I-type plutonic complex ranging from gabbro through diorite to granite	2.8	Jiménez-Munt et al. (2008); Bai et al. (2013), Tunini et al. (2016)
18. Lhasa terrain	Ultramafic rocks. Ordovician and Carboniferous to Triassic shallow marine clastic sediments/melange complexes	2.9–3.0	Jiménez-Munt et al. (2008); Bai et al. (2013); Tunini et al. (2016); Hetényi et al. (2007)
19. Qiangtang terrain	Low to high grade metamorphosed melange complexes	2.651 (2.6–3.0)	Jiménez-Munt et al. (2008); Bai et al. (2013); Tunini et al. (2016)
20. Songpangi terrain	Triassic flysch complex	2.65	Jiménez-Munt et al. (2008); Bai et al. (2013); Tunini et al. (2016)
21. Qaidam basin	Ordovician shallow marine strata interbedded with andesites and volcanic tuffs	2.4	Jiang et al. (2006); Jiménez-Munt et al. (2008); Bai et al. (2013); Tunini et al. (2016)
22. Lithospheric mantle		3.2 [1–3.5e–5 (T–1350°C)]	Jiménez-Munt et al. (2008); Tunini et al. (2016); Afonso et al. (2019)

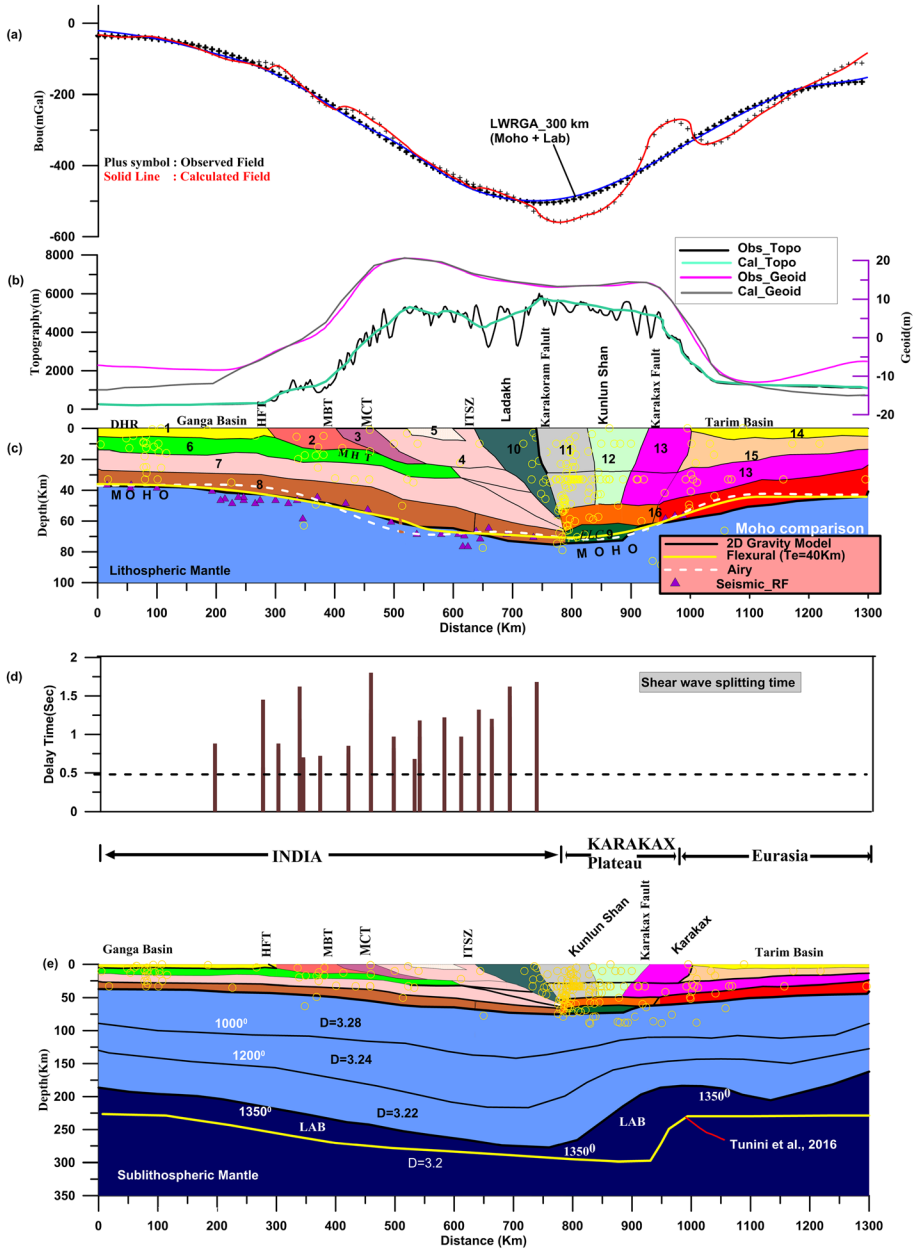

Figure 4. 2-D density model of the crust and upper mantle lithosphere beneath the western part of Himalaya and Tibetan plateau along with profile A-A′ (Figure 1). Panel (a) shows a plot of observed and calculated Bouguer anomalies including long wavelength component (black symbol indicates LWRGA and blue line indicate calculated LWRGA). Panel (b) shows that the elevation along this line shows uniform topography over the Himalaya and Tibetan plateau with the steep gradient at the margins, while geoid undulations show a gradual decrease from south to north with the steep gradient at the margins and are modeled due to deep density heterogeneities arising from undulations in Moho and LAB. Panel (c) shows modeled crustal density structure using constraints from seismic (Magenta triangles; Gilligan et al., 2015; Rai et al., 2006; Wittlinger et al., 2004; Zhang et al., 2014) and geological information (Searle, 2010; Yin & Harrison, 2000). It shows thick crust beneath the Himalaya and Tibetan plateau. A plot of Airy crustal root shows a significant departure from modeled Moho beneath Himalaya and the northern Tibetan plateau. Moho computed from flexural (T_e = 40 km) and modeled from gravity constrained by seismic (RF) are well correlated beneath the Himalaya and southern Tibetan plateau. Panel (d) shows that the plot of delay times (shear wave splitting) shows a gradual increase from south to north excluding some abnormally large scattered values, and panel (e) shows thick lithosphere beneath the Himalaya and thinning of the lithosphere beneath the northern Tibetan plateau. The solid yellow line represents LAB derived from Tunini et al. (2016), which is very close to our profile for comparison. The yellow circle represents earthquakes focal depth distribution (USGS). Physical properties of rocks (numbers) taken Table 1. All abbreviations are the same as in Figure 1.

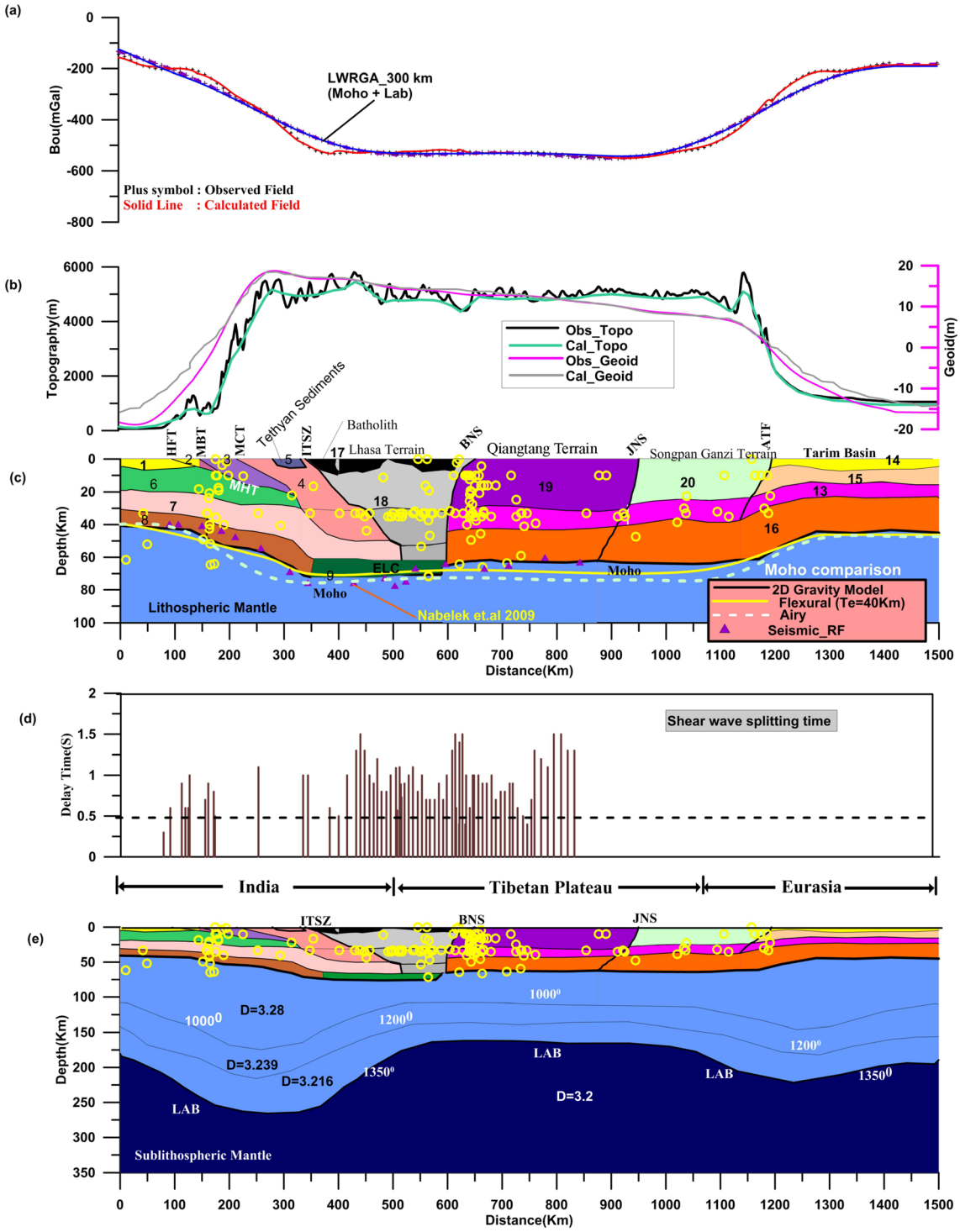

Figure 5. 2-D density structures of the crust and upper mantle lithosphere beneath the central part of the Himalaya and Tibetan plateau along with profile B-B′ (Figure 1). Contents of panels (a) to (d) are the same as described in Figure 4. Crustal and mantle density structures (magenta triangles) are derived from Hetényi et al. (2007), Nabelek et al. (2009), Wittlinger et al. (2009), Basuyau et al. (2013). The results are presented in section 4.1.2. All other abbreviations are the same as in Figure 1.

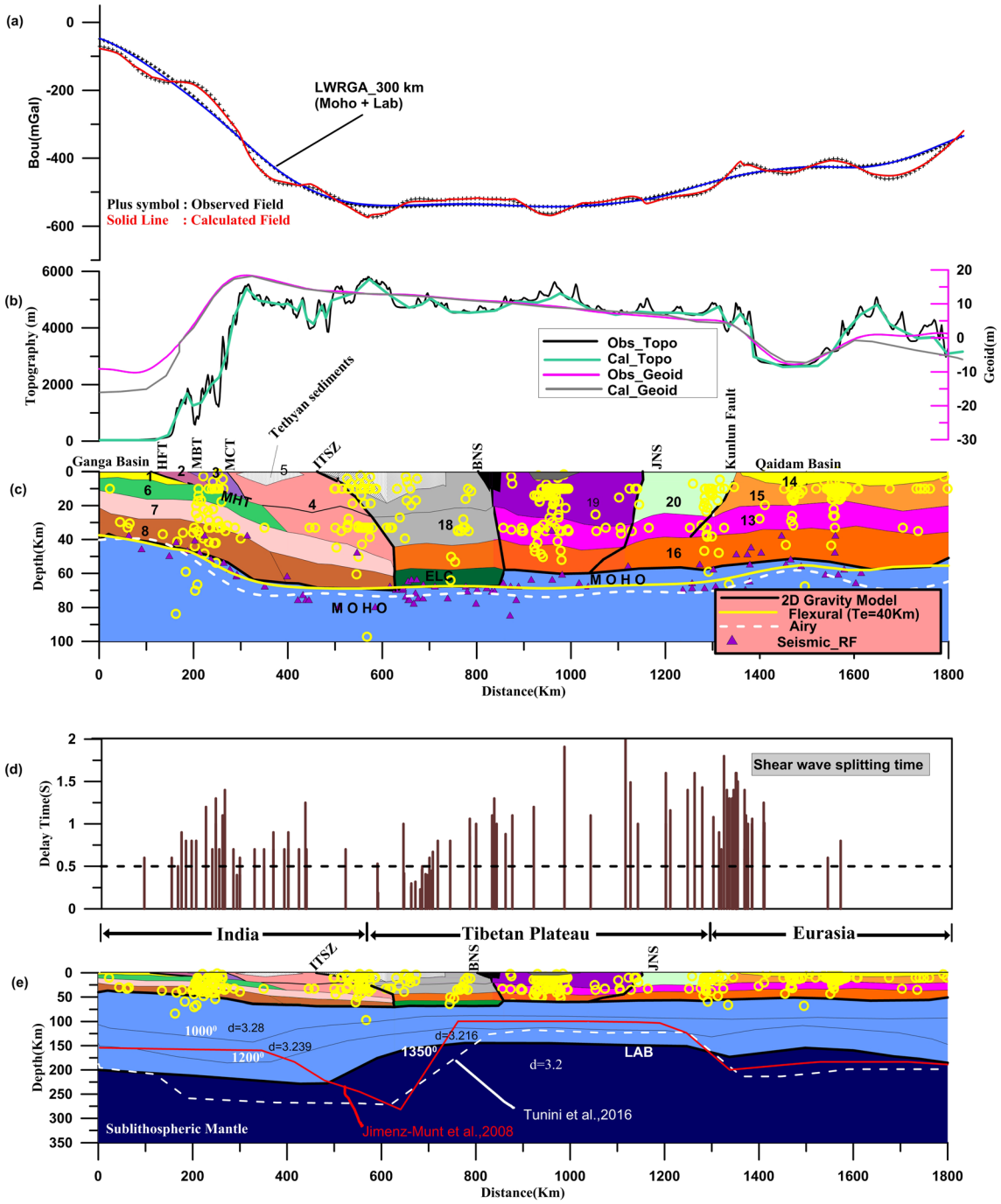

Figure 6. 2-D density structures of the crust and upper mantle lithosphere beneath the eastern part of the Himalaya and Tibetan plateau along with profile C-C′ (Figure 1). Contents of panels (a) to (d) are the same as described in Figure 4. Results are presented in section 4.1.3. All other abbreviations are the same as in Figure 1. Physical properties of crustal bodies (numbers) are adopted from Table 1. All abbreviations are the same as in Figure 1.

Shan (Gilligan et al., 2015; Priestley et al., 2008; Rai et al., 2006; Wittlinger et al., 2004) and a steep reduction in depth to the Moho about ~20 km beyond Karakoram fault (Wittlinger et al., 2004). Based on tomography results, Li et al. (2008) delineated a high-velocity structure beneath the entire Tibetan plateau which also corroborates with the findings of the body wave (Barazangi & Ni, 1982; McNamara et al., 1997), and surface wave studies (Agius & Lebedev, 2013; Lebedev & van der Hilst, 2008; Priestley et al., 2006; Shapiro & Ritzwoller, 2002) depicting underthrusting of the Indian lithosphere beneath western Tibet up to Tarim basin.

Figure 4 shows modeling results along 1,300 km long north-south profile (Figure 1: A-A′) which cuts across the foreland Ganga basin in the south and Tarim basin in the north. The Ganga and Tarim basins show negative Bouguer anomalies due to the presence of low-density thick sediments with the Moho positioned at ~40 km beneath the Ganga basin and ~45 to 50 km beneath the Tarim basin. The input data along the profile shows a steep gradient in elevation and geoid at the margins of the plateau while topography and geoid remain uniform and smooth with values of ~5,000 and ~15 m, respectively, over the Tibetan plateau (Figure 4: panel b). The observed Bouguer gravity anomalies also show steep gradient at the margins with a minimum value of −530 mGal observed in the center of the plateau (Figure 4: panel a). The resultant crustal density model (Figure 4: panel c) shows that the Indian lower crust underthrusts beyond Karakoram fault. The inferred Moho depth shows steep gradient up to MCT, and then the gradient becomes gentle up to Karakoram fault. The crust is 40 to 45 km thick in lesser Himalaya, 50 to 60 km thick in central Himalaya, and 60 to 70 km thick in greater Himalaya (Figure 4: panel c). It shows the most immense crustal thickness (75 km) beneath the Karakorum fault west of the Qiangtang terrain, and the deep earthquakes observed beneath the Karakorum fault appear to be related to the presence of a thick crust in this region (Gilligan et al., 2015; Priestley et al., 2008; Rai et al., 2006). The Tibetan plateau in the west is about 150 to 200 km wide and the north verging Karakax fault separates it from the Tarim basin in the south. Our crustal model (panel c) also shows eclogized dense lower crust (ELC, 3.1 g/cm^3) beneath the Kunlun Shan at a depth of ~70 to 75 km (Rai et al., 2006; Wittlinger et al., 2009) and suggests that the lower Indian crust must be present in partial eclogite (wet) or high-pressure granulite (dry) facies (Priestley et al., 2008; Searle, 2010).

The computed 2-D mantle lithosphere section (Figure 4: panel e) shows a thick lithosphere (250 to 270 km) beneath the Himalayan fold and thrust belt extending beneath the Karakoram. Further north, the lithosphere becomes relatively thin (~180 km) beneath the Karakax plateau where intermediate depth focus earthquakes also occur. Even further north, the lithosphere becomes thick (~200 km) beneath the Tarim basin. Interestingly, the thick lithosphere (down warp in asthenosphere) beneath the Karakoram inferred from gravity modeling supports the results from receiver function (Kumar et al., 2005) and *P* wave tomography (Negredo et al., 2007). Figure 4 (panel d) shows the shear wave splitting delay times plot projected on either side of the profile with a bandwidth of 150 km. It indicates a gradual increase (barring a few scattered values in the south) of shear wave splitting anisotropy from south to north with a sudden jump in delay times toward the north of ITSZ (Oreshin et al., 2008). Interestingly, it coincides with the upwarp of the asthenosphere suggesting the presence of hot and deformed lithosphere in this region between the Indian and Eurasian plate.

4.1.2. Crust and Lithospheric Mantle Structure Beneath the Central Part of Himalaya and Tibetan Plateau

In the central part of the Himalaya-Tibetan plateau collision zone, results from the Hi-CLIMB seismology experiment (Figure 1) across the Himalaya and the southern half of the Tibetan plateau suggest underplating of the Indian lower crust beneath Lhasa block (Hetényi et al., 2007; Nabelek et al., 2009). Also, northward advancement of the Indian lower lithosphere up to the center of the Tibetan plateau (31°N), where it is opposed by the Eurasian lithospheric mantle is documented. Figure 7 shows the observed and computed gravity anomalies and inferred lithospheric density structures along a 1,500 km long N-S trending profile (B-B′) over the central part of the India-Eurasia collision zone. The available geological and geophysical constraints were incorporated in the model from the published results such as crustal geometry from the Hi-CLIMB seismic experiment (Nabelek et al., 2009), crustal density section from Hetényi et al. (2007), and tectonics and geological structures from Yin and Harrison (2000).

Along this profile, from foreland Ganga basin up to ITSZ the gravity field decreases rapidly from −200 to −500 mGal showing a slight increase over the northern plateau. Further north, over the Tarim basin, the gravity field attains the same value as over the Ganga basin. The occurrence of low gravity anomalies due to mantle lithosphere amounts to thinning of the lithosphere resulting in additional uplift of the plateau due to positive buoyancy. The observed elevation and geoid undulations show steep gradient at the margins of the plateau with uniform values in the interior of the plateau. Adopting the same modeling procedure and methodology as employed along with profile A-A′, significant features of the inferred lithosphere density cross-section along profile B-B′ are presented.

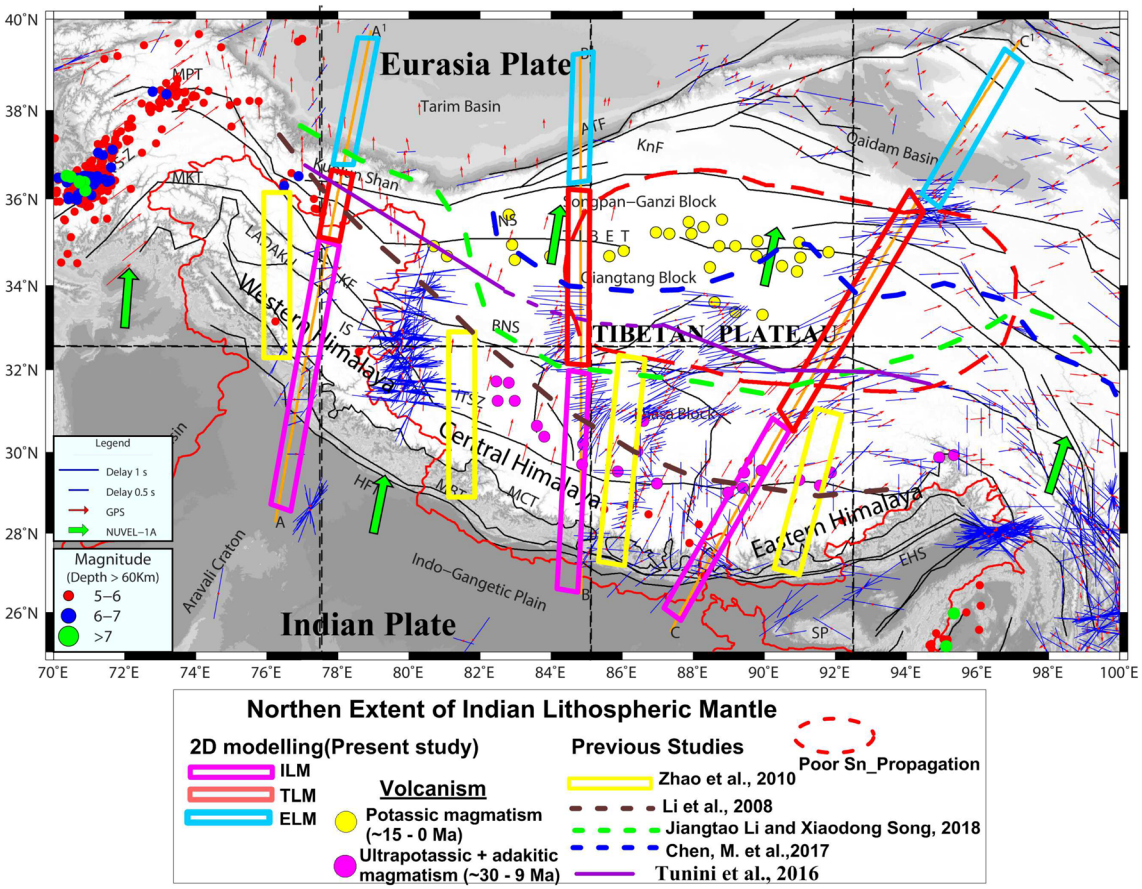

Figure 7. This figure shows previous shear wave splitting measurements (Levin et al., 2008; Oreshin et al., 2008; Sandvol et al., 1997; Wu et al., 2015; Zhao et al., 2010). The rest of the anisotropy data are taken online (http://splitting.gm.univ-montp2.fr/DB/public/searchdatabase.html). Geodetic measurements are derived from Gan et al. (2007) and Pan et al. (2018). The horizontal velocity relative to the stable Eurasian plate throughout the Tibetan plateau suggests that tectonic shortening and crustal thickening are occurring in the southern Tibetan plateau and east west extension in the north-northeastern Tibetan plateau (Ge et al., 2015; Pan et al., 2018). Notice that the excellent correlation between a zone of poor Sn propagation, strong shear wave anisotropy, and associated potassic magmatism of recent period (~15–0 Ma) suggesting the presence of warm and deformed lithosphere in the north-central and northeastern Tibetan plateau. Based on 2-D modeling results, we demarcated the northern edge of the Indian Lithospheric Mantle (ILM), Tibetan Lithospheric Mantle (TLM), and Eurasia Lithospheric Mantle (ELM) of the three modeled profile plotted with the profiles A-A′, B-B′, and C-C′. We also plotted northern edge of the Indian lithospheric mantle from previous tomography and receiver function studies (Li et al., 2008—dark brown dotted line; Tunini et al., 2016—solid purple line; Chen et al., 2017—dotted blue line; Li & Song, 2018—dotted green line; Zhao et al., 2010—yellow box). Our interpretation is close to Li et al. (2008), Zhao et al. (2010), and Li and Song (2018). Yellow and magenta filled circles mark two different episodes of magmatism distributions (Chung et al., 2005, 2009) (See text for details).

The crustal density structure (panel c) shows the presence of thick crust (~78 km) beneath the southern Lhasa terrain, which reduces to ~65 km beneath Qiangtang region of Tibetan plateau with a step in Moho beneath north of Lhasa terrain. It shows a high-density body at ~50 to 70 km depth (ELC, green color, 3.1 g/cm^3) where the reported high V_p/V_s values in Hi-CLIMB main array and is interpreted as underplating of lower continental crust combined with lower crustal eclogitization (Hetényi et al., 2007; Monsalve et al., 2008). The low V_p/V_s (<1.7) values observed beneath the high Himalayan range appear to be related to leucogranites present in the upper crust.

The lithosphere density structure beneath the foreland basin reveals the LAB at a depth of ~170 km which deepens to ~260 km beneath the Himalaya fold and thrust belt. Further north, the LAB becomes thin (~150 km) beneath the northern Lhasa and Qiangtang terrain of the Tibetan plateau. These results suggest the presence of a cold and thick lithosphere beneath the Himalaya and southern part of Tibetan plateau, while northern Tibetan plateau is underlain with a relatively thin and hot lithospheric mantle.

The most prominent feature of the crustal density section beneath the Tibetan plateau is the significant mismatch between the Moho depth derived from gravity modeling on integrating with seismics and the depth predicted from Airy isostasy. This clearly indicates the role of mantle isostasy beneath the Tibetan plateau, which is very evident from the presence of a thin and hot lithosphere beneath the northern part of Tibetan plateau. Thus, the isostatic balance of the observed topography over Himalaya and Tibetan plateau is maintained by the opposing nature of mantle buoyancy. The sudden increase of delay times (>1 s, Figure 5: panel d) over the northern Lhasa and Qiangtang region also points toward the hot and deformable region. Toward the north, LAB beneath Tarim is about 170–200 km depth where the Eurasia lithosphere is subducting southward.

4.1.3. Crust and Lithospheric Mantle Structure Beneath the Eastern Part of Himalaya and Tibetan Plateau

In the eastern of part of Himalaya-Tibetan plateau collision zone, geophysical studies suggest a thin lithosphere mantle located at 150 to 170 km depth beneath the eastern Tibetan plateau compared to northwestern Tibetan plateau where the LAB occurs at a depth of about 220 to 250 km (Jiménez-Munt et al., 2008; Kumar et al., 2006; Shi et al., 2015, 2016; Tunini et al., 2016; Zhao et al., 2010, 2011). Here, we present the results of a joint analysis of gravity, geoid, and elevation data along a NE-SW trending 1,800 km long profile (C-C′) in the eastern sector of the India-Eurasia collision zone. This region is well studied compared to the western and central counterparts. Previous studies in this region suggest deeper Moho (70 to 80 km) beneath southern Lhasa terrane, while crustal thickness in the northern Lhasa terrane varies between 74 and 65 km. Further north, beneath the Qiangtang terrane, the crust thins 60 to 65 km and reduces further 55 to 60 km in the Songpan-Ganzi terrane and Qaidam Basin (Haines et al., 2003; Li et al., 2006; Owens & Zandt, 1997; Zhao et al., 2001).

Interpreted crustal density section (Figure 6: panel c) in the eastern sector also shows significant variation in the Moho depth. Crustal thickness is maximum (75 km) beneath the southern part of the Lhasa block, while Moho is relatively shallow occurring at a depth of ~60 km beneath the Qiangtang and Songpan-Ganzi regions of Tibetan plateau. This model also suggests the presence of high-density (ELC, 3.1 g/cm^3) eclogized rock in the lower crust as inferred for the western and central profiles. The plot of seismicity along the profile shows earthquake clusters along the major faults and thrusts but confined mostly to the crust.

The lithospheric density structure (panel e) shows significant shallowing of the lithosphere-asthenosphere boundary (LAB) in the northern part of the Tibetan plateau where a systematic reduction in Moho depths is also noticed (panel c). The thickness of the lithosphere varies from 200 km beneath the Indian plate to a maximum of 230 km depth beneath the southern Lhasa, which unexpectedly thins down to 140 km under the northern Lhasa and Qiantang terranes. Our results agree with Jiménez-Munt et al. (2008), Tunini et al. (2016), and Afonso et al. (2019).

A very significant feature observed in all the profiles is a relatively higher positive value of geoid undulations over the Himalayan fold belt in the south which decreases to lower values at the northern margin with a gentle gradient over the plateau (Figures 4–6: panel b). This reflects the presence of excess mass resulting from southward thickening of crust and lithosphere and deficit of mass due to thinning of crust and lithosphere toward the north (Figures 4–6: panel e). It may be noted that geoid undulations predominately reflect the deep-seated density heterogeneities compared to Bouguer gravity anomalies. The modeled geoidal undulations show excellent match between the observed and calculated anomalies over the Himalaya and Tibetan plateau which is the region of our interest. However, it shows a misfit at both ends of the profiles which may be caused due to the edge effects of the anomalous upper mantle density heterogeneities away from the region of our study. Due to the lack of enough geophysical constraints, we did not model them to reduce the misfit.

We modeled topography (Figures 4–6: panel b) along with the gravity and geoid undulations to determine the depth to the Moho and thickness of the lithosphere. The computed elevations matched well with the observed topography over the interior of the plateau. Unlike the uniform topography over the interior of the plateau, thickness of the crust and lithosphere differ from southern Tibetan plateau to the northern Tibetan plateau, which is very well reflected in the lithospheric density model (Figures 4–6: panel e). Despite this variation, the presence of near zero free-air anomalies over the interior of the plateau point

toward complete isostatic compensation. The topography of the western Tibetan plateau is somewhat higher (5,000 m) compared to the eastern Tibetan plateau (4,500 m) which is significantly narrower (400 km) than the eastern Tibetan plateau (1,000 km). The variation in the geometry of the India-Eurasia plate collision zone explains the differences in surface topography between the western and eastern parts of Tibetan plateau.

Figure 6 (panel d) also shows shear wave splitting delay time data extracted along the profile with a band width of 150 km on either side of the profile. The causes of anisotropy are usually associated with finite strain such as the preferred orientation of minerals like olivine due to flow in the mantle or the lower crust, metamorphic fabrics, or fracture patterns. Measurements of SKS birefringence (delay time, δt) which is mainly caused by finite strain in the lithospheric mantle shows a significant jump in δt values on the order 0.8 to 1.2 s from the background. To explain this, step-like increase in δt, we require the presence of a 100 to 144 km thick lithospheric mantle in the region (Silver & Chan, 1991). Such a rapid change or increase cannot be reconciled easily with the observed uniform thickness of the lithosphere in this region. McNamara et al. (1994) suggested that large anisotropy in the northern Tibetan plateau is the reflection of E-W deformation fabric in the mantle due to N-S shortening of the Tibetan lithosphere. However, asthenospheric flow-induced anisotropy could be an alternative explanation where a weak asthenosphere flows eastward in response to compression between converging strong and thick Indian and Eurasian lithosphere. Furlong and Owens (1997) suggested that anisotropy may be attributed to a combination of sublithospheric mantle flow and lithospheric fabric associated with the south dipping Eurasian lithosphere. We suggest that a sudden increase in the delay time (>2 s) in northern Lhasa and Qiangtang terrain might be due to mantle flow and favor the earlier perception of a weak, deformable, and hot mantle lithosphere in this region. In this context, we have computed the effective elastic thickness of the lithosphere (T_e) described in the methodology section 3.2 to understand the flexural strength of the lithosphere, which in turn may throw light on the nature of the deformation within the lithosphere.

4.2. Effective Elastic Thickness (T_e): Implications on Lithospheric Structure

The estimated T_e values (Figure 2, see blocks) are invariably high (~55 km) over the Indian shield region and agree with the estimates of Lyon-Caen and Molnar (1983), Caporali (1995), Jiang et al. (2004), and Tiwari et al. (2008). In the northern Tibetan plateau, T_e values are generally low (<30 km) within Qiangtang (Block 3) and northeastern Tibet (Block 4) and agree with the estimates of Cattin et al. (2001), Braitenberg et al. (2003), and Chen et al. (2015). Hetényi et al. (2006), with constraints on the crustal thickness from receiver function analysis and INDEPTH results suggested a decrease in T_e from 60–80 km under foreland to 20–30 km further north as it is flexed down beneath the Himalaya and Tibetan plateau. Jordan and Watts (2005) based on detailed analysis of Bouguer anomaly and topography suggested variations of effective elastic thickness (T_e) ranging from 70 km in the central region of foreland Ganga basin to 30–50 km toward the east and the west.

The presence of low T_e values over northern Tibetan plateau (Figure 2, Blocks 3 and 4) indicates that the lithosphere is thin in this region. This correlates well with the presence of recent (<6 Ma) potassic and adakitic volcanism (Figure 7). The thinning of the lithosphere would explain the low P, Pn velocity (McNamara et al., 1995), and inefficient Sn propagation (Barazangi & Ni, 1982; McNamara et al., 1995), high-Poisson's ratio (Owens & Zandt, 1997), low T_e (T_e < 30 km, Chen et al., 2015, and present study), east and southeast oriented global positioning system displacements (Figure 7); large birefringence of *S* waves (McNamara et al., 1994), up to 2 s or more between fast- and slow-directions of polarization inferred as a result of east-west flow in the upper mantle observed in this region (Owens & Zandt, 1997) high electrical conductivities suggesting a hot and deformable environment throughout crust and mantle (Yue et al., 2012). It also corresponds to the widespread low-resistivity zones in the crust indicating the presence of fluid or melts derived from fractional melting of the lithospheric mantle (Unsworth et al., 2004; Wang et al., 2016; Wei et al., 2001). Based on thermal modeling, Artemieva (2006) also predicts higher temperatures beneath north-east Tibetan plateau than in the south. The estimated lithospheric thickness, according to Artemieva (2006), varies from 180 km beneath southern Tibetan plateau to 125 km beneath NE Tibetan plateau. The warm and weak layers in the lower crust and the upper mantle in the northern Tibetan plateau appear to facilitate an easterly escape of the whole lithosphere; such eastward movement is confirmed by GPS data (Ge et al., 2015; Pan et al., 2018; Zhang et al., 2004).

5. Discussions

5.1. State of Isostasy Beneath Himalaya and Tibetan Plateau

The Himalaya and Tibetan plateau constitute the highest mountains and highest plateau on the surface of the earth, respectively, and are underlain by thick lithosphere associated with high-velocity upper mantle anomalies beneath the Himalaya and southern Tibetan plateau. However, the northern Tibetan plateau is associated with a thin lithosphere low-velocity upper mantle anomalies. These contrasting observations suggest an intimate relationship between mantle geodynamic processes and surface topography. The presence of near zero free-air gravity anomalies over the Tibetan region suggests that it is in isostatic equilibrium. This study reveals that Airy-type isostatic Moho departs from the Moho derived from seismic and gravity modeling beneath the Himalaya and Tibetan plateau. The Moho derived from flexural modeling ($T_e = 40$ km) and that modeled from gravity with constraints from receiver function results are well correlated (Figures 4–6: panel c). Hence, the Himalaya shows local deviations from Airy isostasy and suggests a different mode of compensation (Cattin et al., 2001; Hetényi et al., 2006; Tiwari et al., 2006). In the Himalayas it is undercompensated, whereas in Ganga basin it seems overcompensated, as reflected in the 2-D crustal density sections. Thus, the suggested regional flexural model seems appropriate for Himalayan topography and is most likely related to the underthrusting and flexing down of the Indian lithosphere beneath the higher Himalaya's with an extension toward southern Tibetan plateau resulting in thickening of the lithosphere and the crust.

As explained by Molnar et al. (1993), horizontal shortening due to continental collision would produce not only a thickened crust but also results in thickening of the cold lithosphere which will be dense compared to the surrounding asthenosphere at the same depth. Therefore, buoyancy due to crustal root appears to hold the topography high, whereas negative buoyancy due to lithospheric root would reduce isostatic uplift of the thickened crust and must have resulted in slight deepening of the Moho as observed in 2-D density models in the southern side beneath the Himalayan mountains. However, thinning of the lithosphere due to convective removal of the thickened lithosphere because of Rayleigh-Taylor instability would result in higher temperature in the lithospheric mantle due to asthenospheric upwelling and the resultant buoyancy would not only uplift the surface but also upwarp the Moho topography as observed in the 2-D sections beneath the northern plateau (Figures 4–6). This indicates that the entire lithosphere is involved in isostatic compensation of the Himalaya and Tibetan plateau, although significant contribution comes from the Moho undulations.

Therefore, it is recognized that in spite of uniform elevation of Tibetan plateau, the mode of isostatic compensation over its southern and northern parts is entirely different. As a consequence of this, Tibetan plateau underwent two stages of uplift (i) during the thickening of the crust due to N-S shortening of the Tibetan crust and (ii) during the thinning of the Tibetan lithosphere due to convective removal of the thickened lithosphere and asthenospheric upwelling. Uplift during stage (i) is slow but has a larger amplitude (~3.5 to 4.0 km), while during stage (ii) uplift is rapid, but amplitude is small (~1.5 km). A similar inference was also drawn by Molnar et al. (1993) and Jiménez-Munt et al. (2008).

5.2. Lower Crustal Eclogitization Process Beneath Himalaya and Lhasa Terrain

The presence of high density lower crustal rocks at a depth of 60 to 75 km above the Moho is a distinct feature observed in all the profiles (Figures 4–6) and is attributed to eclogites. Compared to the western profile (Figures 4: panel a), the central and eastern profiles (Figures 5 and 6: panel a), show local raise of gravity north of the ITSZ, beneath the Lhasa terrain, which is a sign of eclogized high density material (panel c). Our results are also consistent with previous 2-D gravity models with a eclogized high density layer beneath the Lhasa terrane north of the ITSZ (Hetényi et al., 2007; Tiwari et al., 2006). Also, Schulte-Pelkum et al. (2005) reported delineation of a high velocity region in the Indian lower crust toward northern part of the Himalayas characterized as eclogite, which is high-density material, affecting the dynamics of the Tibetan plateau.

Previous studies have also shown that eclogitization of the lower crust is a key process in support of high topographic elevation of both Himalayas and Tibetan plateau (Bousquet et al., 1997; Henry et al., 1997). The presence of fast lower-crustal *P* wave velocities based on receiver functions, Schulte-Pelkum et al. (2005) argued that the lower crust is partially (~30%) eclogitized just south of the Yarlung Tsangpo Suture (YTS) and that the eclogitization process is governed by water availability. This implies that the lower crustal

material reaches the eclogite facies via granulite facies conditions, as shown in Le Pichon et al. (1997) for geotherms established after more than ~20 Myr of relaxation. However, the latter study also indicates that the geotherm may follow an amphibolite eclogite and even a blue schisteclogite path for shorter relaxation times between ~10–20 Myr and less than ~10 Myr, respectively. The formation of eclogite is accompanied by copious fluids (Hetényi et al., 2007), and evidence for which is also noticed in the form of high conductive anomalies and seismic bright spots in the lower crust under the Himalaya and southern Tibetan plateau (Brown et al., 1996; Unsworth et al., 2005; Zhang et al., 2014). Furthermore, evidence of high P wave velocity (Schulte-Pelkum et al., 2005; Shi et al., 2015, 2016), high density (Hetényi et al., 2007), and high V_p/V_s ratios (Hetényi et al., 2007; Nabelek et al., 2009) suggests that the Indian lower crust has acquired variable degrees of eclogitization beneath the southern Lhasa terrane. Therefore, the presence of eclogites in the lower crust appears to be a characteristic signature of the Himalayan tectonic zone which might have facilitated delamination and detachment as suggested by Leech (2001).

5.3. Nature of Lithospheric Mantle and Volcanism

The upper mantle density distribution inferred from constrained potential field modeling along the India-Eurasia collision zone (Figures 4–6) reveals distinct mantle anomaly contributions over the Tibetan plateau to the north and the Himalayan fold belt in the south. Mantle anomaly contribution is negative over the northern part of Tibetan plateau due to upwarp of the hot asthenosphere. This has resulted in thinning of the mantle lithosphere to produce positive mantle buoyancy in this region. However, mantle anomaly contribution is positive over the Himalayan fold belt due to the presence of a thick mantle lithosphere which produced negative mantle buoyancy.

The anomalous zone of thin lithosphere is narrow over the Kunlun Shan in the west and broad in the central and eastern parts encompassing the northern part of Lhasa, Qiangtang, and Songpan Ganzi terrain of the Tibetan plateau. It also coincides with low T_e value (<30 km) and shows excellent association with post-collisional (15 to 0 Ma). Cenozoic and Recent potassic volcanic rocks on the surface (Figure 7), whereas ultrapotassic and adakitic rocks of age (~30 to 9 Ma) are distributed in the south slightly away from the zone of low T_e and thin lithosphere. These volcanic rocks irrespective of their locations are chemically and isotopically similar (Miller et al., 1999; Turner et al., 1996) and are generally potassic and strongly enriched in incompatible elements (Chung et al., 2009; Cooper et al., 2002; Zhang et al., 2008). It is suggested that these alkaline volcanic rocks are produced due to partial melting of the thinned mantle lithosphere due to asthenospheric upwelling (Xia et al., 2011). However, the lack of recent volcanism in the southern part of this anomalous low T_e and thin lithosphere is intriguing. The presence of cold and thick Indian lithosphere inferred beneath this zone must have prevented the recent magmatism in this region which is in agreement with the tectonic model proposed by Xia et al. (2011) based on age and petrochemistry of Cenozoic volcanic rocks from Tibetan plateau.

5.4. Northern Extent of Indian Lithosphere Beneath the Himalaya-Tibetan Plateau and Its Geodynamic Implications

Based on the integration of 2-D modeled lithospheric density cross sections (Figures 4–6: panel e), we have demarcated the northern front of the underthrusting Indian lithosphere and compared with previous results (Figure 7). In the western sector, the Indian lithosphere underthrusts up to Karakoram fault, and it extends up to the south of BNS beneath the central region. While in the eastern region it continues up to ITSZ (Figure 7). Our results are in consonance with earlier studies in the northern front of the Indian lithosphere based on seismic tomography and receiver function analysis (Kumar et al., 2006; Li et al., 2008; Zhao et al., 2010, 2011). Based on previous tomography models (Li et al., 2008; Replumaz et al., 2013; Tilmann et al., 2003), Chen et al. (2017) proposed underthrusting of the Indian lithospheric mantle coinciding with the Jinsa Nujiang Suture (Figure 7, blue dotted line), which extends too far northward. Li and Song (2018), based on P and S wave tomography images also suggested that the subducted Indian mantle lithosphere is torn into four pieces with different angles and with different northern limits. They indicated that in the central part it is steeper and extends to BNS (Figure 7, green dotted line), where as in the west and east it extends further with a gentle dip. Our 2-D density modeling results also reveal that in the west, the Indian lithosphere underthrusts/subducts horizontally up to the Karakoram at a low angle. In the central region it is subducting at a high angle till south of the BNS, whereas in the east it again subducts at a shallow angle reaching ITSZ and possibly up to south of the BNS (Figures 4–6: panel e). The geometry of

the India and Eurasia plate collision zone also explains the differences in surface topography between the west and east parts of Tibet. The more rugged and high topography observed in western Tibet can be supported by the rigid mantle lithosphere, whereas to the east, the lithosphere is weaker due to the existence of the crush zone, which is also seen in spatial variations of T_e reducing from west to east. A large number of shear wave splitting (SWS) studies (Figure 7) also reveal that the mantle deformation in the western Tibetan plateau is entirely different from that in the east. (e.g., Chen et al., 2010; Gao & Liu, 2009; Huang et al., 2000; McNamara et al., 1994; Sandvol et al., 1997; Zhao et al., 2010).

Finally, the 2-D lithospheric structures obtained in this study provide tight constraints on the geodynamic evolution of the Himalayan-Tibetan orogen. Our lithospheric density structures suggest that firstly, the deformation of the Tibetan lithosphere started with the shortening of the lithosphere due to continued convergence between India and Eurasia plates after their collision at ~50 Ma (Houseman & England, 1993; Molnar et al., 1993). This resulted in thickening of the crust and lithospheric mantle and initial upwarp of the Tibetan plateau. Subsequently the lithospheric root beneath the thickened crust of Tibetan plateau was removed owing to Rayleigh-Taylor instability during the Oligocene and is replaced with upwelling of hot and light asthenosphere. This resulted in the rapid upwarp of the Tibetan plateau which is in agreement with the geodynamic model of Houseman and England (1993), Molnar et al. (1993), Jiménez-Munt and Platt (2006), and Xia et al. (2011). The presence of a thick crust with a thick lithospheric root beneath the Himalaya and southern part of Tibetan plateau favored the northward underthrusting of the cold Indian mantle lithosphere at the onset of asthenospheric upwelling. The cold Indian plate appears to have reached the southern part of Tibetan plateau by such time (Oligocene) and thus shut off the heat source from the asthenosphere. As a consequence of this underthrusting of Indian lithosphere no igneous activity younger than this age occurs in the southern Tibetan plateau, whereas the alkaline potassic volcanism caused by the destruction and the removal of the thickened lithosphere in the northern Tibetan plateau continued to the present time.

6. Conclusions

The results obtained in this study allow us to make the following conclusions.

The most significant and noteworthy result of our contribution is delineation of the geometry of the lithosphere-asthenosphere boundary (LAB) beneath Himalaya and Tibetan plateau. 2-D modeling results and lateral variation of T_e reveals significant excursions in the thickness of the lithosphere from south to north beneath the Himalaya and Tibetan plateau. In the western part of the India-Eurasia collision zone, lithosphere is thick (~200–250 km) beneath the Himalaya and the Karakoram fault and gradually thins to (~160 km) beneath the Kunlun Shan and Karakax plateau and again increases to more than 200 km beneath the Tarim basin. In the central part of Himalaya-Tibetan plateau, the LAB shows significant variation in depths starting from 145–160 km beneath the foreland basin to 200–240 km beneath the Himalaya and reaching ~250 km beneath the Lhasa terrain to the south of the BNS. Further north, beneath the Qiangtang and Songpan Ganzi region, we observed significant thinning (130–140 km) of the LAB and then an increase to ~180–200 km beneath the ATF and Tarim basin. In the eastern Himalaya-Tibetan region, our results suggest thick lithosphere beneath the Himalaya that extends up to the north of ITSZ (30.5°N). Further north, beneath the Lhasa, we observe a thin lithosphere (~140–160 km) which extends up to eastern Qiangtang and Songpong-Ganzi regions. Based on the integration of 2-D modeled lithospheric density cross sections, we have demarcated the northern front of the underthrusting Indian lithosphere. In the western sector, the Indian lithosphere underthrusts up to Karakoram fault, and it extends up to the south of BNS beneath the central region. Whereas in the eastern region it continues up to ITSZ.

The results of our study also reveal significant variations in subcrustal lithospheric mantle thickness that mimic the differences in crustal thickness (Moho depth) suggesting that the entire lithosphere provides the required buoyancy to maintain the nearly uniform elevation of the Tibetan plateau.

Our T_e variations reveal first-order differences in the mechanical character and structure between southern and northern Tibet. The excellent agreement between T_e and 2-D modeling results suggest that the spatial variations of T_e values offer an alternative possibility to explain the flexural strength of the lithosphere and northern extent of the underthrusting Indian lithosphere. Thinner lithosphere and low T_e (~<30 km)

under northern Tibetan plateau indicate predominance of mantle isostasy where the crust and mantle are anomalously hot and deformable which also correlates well with low seismic velocity, strong shear wave anisotropy (>2 s) and eastward crustal flow as observed in GPS data.

In general, our lithospheric density structures in this study are derived from 2-D modeling of geopotential data and are restricted along the strike of the India-Eurasia collision zone. This therefore warrant further investigations using 3-D modeling approaches to arrive at 3-D density distribution and effective elastic thickness leading to a better geophysical model. The work in this direction is under progress.

Data Availability Statement

The topography data are taken from Becker et al. (2009; https://topex.ucsd.edu/cgi-bin/get_srtm30.cgi). Gravity data are downloaded from Ries et al. (2016; http://doi.org/10.5880/icgem.2016.002). The geoid data are taken from Pavlis et al. (2012), Global model: EGM2008. Anisotropy data are taken online (http://splitting.gm.univ-montp2.fr/DB/public/searchdatabase.html). GPS data used in this study are from Gan et al. (2007) and Pan et al. (2018). Some of the figures are generated with the Generic Mapping Tools software (Wessel & Smith, 1995).

Acknowledgments

M. R. K. thanks the Director of Indian Institute of Geomagnetism (IIG), Mumbai, and the Director of CSIR-National Geophysical Research Institute (CSIR-NGRI), Hyderabad, for their encouragement and permission to publish this work. We are thankful to Ajay Kumar of the Group Dynamics of the Lithosphere (GDL), Institute of Earth Science Jaume Almera, Spain, for his fruitful discussions regarding mineral properties and help during installation of LitMod-2D_2.0 software package. We are grateful to the Editor, Prof. Geissman, and associate editor, Dr. Claire Currie, for their encouragement and anonymous reviewers for their critical and fruitful comments for improving the manuscript. M. R. K. thank Dr. A. P. Singh, Head Gravity and Magnetic Studies Group, NGRI, for his continuous support. This work is permitted to publish with reference number NGRI/Lib/2020/Pub-107.

References

Acton, C. E., Priestley, K., Gaur, V. K., & Rai, S. S. (2010). Group velocity tomography of the Indo-Eurasian collision zone. *Journal of Geophysical Research*, *115*, B12335. https://doi.org/10.1029/2009JB007021

Afonso, J. C., Fernandez, M., Ranalli, G., Griffin, W. L., & Connolly, A. D. (2008). Integreted geophysical petrological modelling of the lithosphere and sub-lithospheric upper mantle: Methodology and applications. *Geochemistry, Geophysics, Geosystems*, *9*, Q0508. https://doi.org/10.1029/2007GC001834

Afonso, J. C., Salajegheh, F., Szwillus, W., Ebbing, J., & Gaina, C. (2019). A global reference model of the lithosphere and upper mantle from joint inversion and analysis of multiple data sets. *Geophysical Journal International*, *217*(3), 1602–1628. https://doi.org/10.1093/gji/ggz094

Afonso, J. C., & Zlotnik, S. (2011). The subductability of continental lithosphere: The before and after story. *Frontiers in Earth Science*, 53–86. https://doi.org/10.1007/978-3-540-88558

Agius, M. R., & Lebedev, S. (2013). Tibetan and Indian lithospheres in the upper mantle beneath Tibet: Evidence from broadband surface-wave dispersion. *Geochemistry, Geophysics, Geosystems*, *14*, 4260–4281. https://doi.org/10.1002/ggge.20274

Airy, G. B. (1855). On the computation of the effect of the attraction of mountain-masses, as disturbing the apparent astronomical latitude of stations in geodetic surveys. *Philosophical Transactions. Royal Society of London*, *145*, 101–104.

Allegre, C. J., Courtillot, V., Tapponnier, P., Hirn, A., Mattauer, M., Coulon, C., et al. (1984). Structure and evolution of the Himalaya-Tibet orogenic belt. *Nature*, *307*(5946), 17–22. https://doi.org/10.1038/307017a0

Andersen, O. B., Knudsen, P., Stenseng, L., Kenyon, S. C., Factor, J. K., Markiel, N., & Ingalls, S. (2014). *The global gravity field model (DTU13) and evaluation in the Arctic Ocean*. Paper presented at third international symposium of the gravity field of the Earth (IGFS3), Shanghai, China.

Artemieva, I. M. (2006). Global 1°×1° thermal model TC1 for the continental lithosphere: Implications for lithosphere secular evolution. *Tectonophysics*, *416*(1–4), 245–277. https://doi.org/10.1016/j.tecto.2005.11.022

Audet, P., Jellinek, A. M., & Uno, H. (2007). Mechanical controls on the deformation of continents at convergent margins. *Earth and Planetary Science Letters*, *264*(1–2), 151–166. https://doi.org/10.1016/j.epsl.2007.09.024

Bagherbandi, M. (2011). A comparison of three gravity inversion methods for crustal thickness modelling in Tibet plateau. *Journal of Asian Earth Sciences*, *43*, 89–97.

Bai, Z., Zhang, S., & Braitenberg, C. (2013). Crustal density structure from 3D gravity modeling beneath Himalaya and Lhasa blocks, Tibet. *Journal of Asian Earth Sciences*, *78*, 301–317. https://doi.org/10.1016/j.jseaes.2012.12.035

Barazangi, M., & Ni, J. (1982). Velocities and propagation characteristics of Pn and Sn beneath the Himalayan arc and Tibetan plateau: Possible evidence for underthrusting of Indian continental lithosphere beneath Tibet. *Geology*, *10*(4), 179–185. https://doi.org/10.1130/0091-7613(1982)10<179:VAPCOP>2.0.CO;2

Basuyau, C., Diament, M., Tiberi, C., Hetenyi, G., Vergne, J., & Peyrefitte, A. (2013). Joint inversion of teleseismic and GOCE gravity data: Application to the Himalayas. *Geophysics Journal International*, *193*(1), 149–160. https://doi.org/10.1093/gji/ggs110

Becker, J. J., Sandwell, D. T., Smith, W. H. F., Braud, J., Binder, B., Depner, J., et al. (2009). Global bathymetry and elevation data at 30 arc seconds resolution: SRTM30_PLUS. *Marine Geodesy*, *32*(4), 355–371. https://doi.org/10.1080/01490410903297766

Bousquet, R., Goffé, B., Henry, P., Le Pichon, X., & Chopin, C. (1997). Kinematic, thermal and petrological model of the Central Alps: Lepontine metamorphism in the upper crust and eclogitisation of the lower crust. *Tectonophysics*, *273*(1–2), 105–127. https://doi.org/10.1016/S0040-1951(96)00290-9

Bowin, C. (1983). Depth of principal mass anomalies contributing to the Earth's geoidal undulations and gravity anomalies. *Marine Geodesy*, *7*(1–4), 61–100. https://doi.org/10.1080/15210608309379476

Bowin, C. (2000). Mass anomaly structure of the earth. *Reviews of Geophysics*, *38*(3), 355–387. https://doi.org/10.1029/1999RG000064

Braitenberg, C., Wang, Y., Fang, J., & Hsu, H. T. (2003). Spatial variations of flexure parameters over the Tibet–Quinghai plateau. *Earth and Planetary Science Letters*, *205*, 211–224. https://doi.org/10.1016/S0012-821X(02)01042-7

Braitenberg, C., Zadro, M., Fang, J., Wang, Y., & Hsu, H. T. (2000). The gravity and isostatic Moho undulations in Qinghai-Tibet plateau. *Journal of Geodynamics*, *30*(5), 489–505. https://doi.org/10.1016/S0264-3707(00)00004-1

Brown, L. D., Zhao, W., Nelson, K. D., Hauck, M., Alsdorf, D., Ross, A., et al. (1996). Bright spot, structure and magmatism in southern Tibet from INDEPTH seismic reflection profiling. *Science*, *274*(5293), 1688–1690. https://doi.org/10.1126/science.274.5293.1688

Caporali, A. (1995). Gravity anomalies and the flexure of the lithosphere in the Karakoram, Pakistan. *Journal of Geophysical Research*, *100*(B8), 15,075–15,085. https://doi.org/10.1029/95JB00613

Cattin, R., Martelet, G., Hentry, P., Avouac, J. P., Diament, M., & Shakya, T. R. (2001). Gravity anomalies, crustal structure and thermomechanical support of the Himalaya of Central Nepal. *Geophysical Journal International*, *147*(2), 381–392. https://doi.org/10.1046/j.0956-540x.2001.01541.x

Chen, B., Liu, J., Chen, C., Du, J., & Sun, Y. (2015). Elastic thickness of the Himalayan-Tibetan orogen estimated from the fan wavelet coherence method, and its implications for lithospheric structure. *Earth and Planetary Science Letters*, *409*, 1–14. https://doi.org/10.1016/j.epsl.2014.10.039

Chen, M., Niu, F., Tromp, J., Lenardic, A., Lee, C. T. A., Cao, W., & Ribeiro, J. (2017). Lithospheric foundering and underthrusting imaged beneath Tibet. *Nature Communications*, *8*(1), 15659. https://doi.org/10.1038/ncomms15659

Chen, W. P., Martin, M., Tseng, T., Nowack, R. L., Hung, S., & Huang, B. (2010). Shear-wave birefringence and current configuration of converging lithosphere under Tibet. *Earth and Planetary Science Letters*, *295*(1–2), 297–304. https://doi.org/10.1016/j.epsl.2010.04.017

Chung, S. L., Chu, M. F., Ji, J., O'Reilly, S. Y., Pearson, N. J., Liu, D., et al. (2009). The nature and timing of crustal thickening in southern Tibet: Geochemical and zircon Hf isotopic constraints from postcollisional adakites. *Tectonophysics*, *477*(1–2), 36–48. https://doi.org/10.1016/j.tecto.2009.08.008

Chung, S. L., Chu, M. F., Zhang, Y., Xie, Y., Lo, C. H., Lee, T. Y., et al. (2005). Tibetan tectonic evolution inferred from spatial and temporal variations in post-collisional magmatism. *Earth-Science Reviews*, *68*(3–4), 173–196. https://doi.org/10.1016/j.earscirev.2004.05.001

Coblentz, D., Chase, C. G., Karlstrom, K. E., & van Wijk, J. (2011). Topography, the geoid, and compensation mechanisms for the southern Rocky Mountains. *Geochemistry, Geophysics, Geosystems*, *12*, Q04002. https://doi.org/10.1029/2010GC003459

Connolly, J. A. D. (2005). Computation of phase equilibria by linear programming: A tool for geodynamic modeling and its application to subduction zone decarbonation. *Earth and Planetary Science Letters*, *236*(1–2), 524–541. https://doi.org/10.1016/j.epsl.2005.04.033

Cooper, K. M., Reid, M., Dunbar, N. W., & McIntosh, W. C. (2002). Origin of mafic magmas beneath northwestern Tibet: Constraints from Th-U disequilibria. *Geochemistry, Geophysics, Geosystems*, *3*(11), 1065. https://doi.org/10.1029/2002GC000332

Deng, W., Zheng, X., & Matsumoto, Y. (1996). Petrological characteristics and ages of Cenozoic volcanic rocks from the Hoh Xil Mts., Qinghai Province. *Acta Petrologica et Mineralogica*, *15*, 289–298.

Dewey, J. F., Shackleton, R. M., Chang, C., & Sun, Y. (1988). The tectonic evolution of the Tibetan plateau. *Philosophical Transactions of the Royal Society of London*, *327*(1594), 379–413. https://doi.org/10.1098/rsta.1988.0135

England, P. C., & Houseman, G. A. (1989). Extension during continental convergence, with application to the Tibetan plateau. *Journal of Geophysical Research*, *94*, 17,561–17,579.

Forsyth, D. W. (1985). Subsurface loading and estimate of the flexural rigidity of continental lithosphere. *Journal of Geophysical Research*, *90*(B14), 12,623–12,632. https://doi.org/10.1029/JB090iB14p12623

Fullea, J., Fernàndez, M., & Zeyen, H. (2008). FA2BOUG—A FORTRAN 90 code to compute Bouguer gravity anomalies from gridded free-air anomalies: Application to the Atlantic-Mediterranean transition zone. *Computers and Geosciences*, *34*(12), 1665–1681. https://doi.org/10.1016/j.cageo.2008.02.018

Furlong, K. P., & Owens, T. J. (1997). Lithospheric mantle rollback beneath northern Tibet: Evidence from mantle anisotropy (abstract). *Geological Society of America Bulletin*, *29*(144), 1997.

Galve, A., Jiang, M., Hirn, A., Sapin, M., Laigle, M., de Voogd, B., et al. (2006). Explosion seismic P and S velocity and attenuation constraints on the lower crust of the north–central Tibetan plateau, and comparison with the Tethyan Himalayas: Implications on composition, mineralogy, temperature, and tectonic evolution. *Tectonophysics*, *412*(3–4), 141–157. https://doi.org/10.1016/j.tecto.2005.09.010

Gan, W., Zhang, P., Shen, Z. K., Niu, Z., Wang, M., Wan, Y., et al. (2007). Present-day crustal motion within the Tibetan plateau inferred from GPS measurements. *Journal of Geophysical Research*, *112*, B08416. https://doi.org/10.1029/2005JB004120

Gao, C., & Ye, D. (1997). Petroleum geology of the Tarim Basin, NW China: Recent advances. *Journal of Petroleum Geology*, *20*(2), 239–244.

Gao, S. S., & Liu, K. H. (2009). Significant seismic anisotropy beneath the southern Lhasa Terrane, Tibetan plateau. *Geochemistry, Geophysics, Geosystems*, *10*, Q02008. https://doi.org/10.1029/2008GC002227

Ge, W. P., Molnar, P., Shen, Z. K., & Li, Q. (2015). Present-day crustal thinning in the southern and northern Tibetan plateau revealed by GPS measurements. *Geophysical Research Letters*, *42*, 5227–5235. https://doi.org/10.1002/2015GL064347

Gilligan, A., Priestley, K. F., Roecker, S. W., Levin, V., & Rai, S. S. (2015). The crustal structure of the western Himalayas and Tibet. *Journal of Geophysical Research: Solid Earth*, *120*, 3946–3964. https://doi.org/10.1002/2015JB011891

GM-SYS (2000). Gravity/magnetic modelling software, version4.6, *Northwest Geophysical Assoc., Inc., U.S.A.*

Guillot, S., Garzanti, E., Baratoux, D., Marquer, D., Maheo, G., & de Sigoyer, J. (2003). Reconstructing the total shortening history of the NW Himalaya. *Geochemistry, Geophysics, Geosystems*, *4*(7), 1064. https://doi.org/10.1029/2002GC000484

Haines, S. S., Klemperer, S. L., Brown, L., Jingru, G., Mechie, J., Meissner, R., et al. (2003). INDEPTH III seismic data: From surface observations to deep crustal processes in Tibet. *Tectonics*, *22*(1), 1001. https://doi.org/10.1029/2001TC001305

Hauck, M. L., Nelson, K. D., Brown, L. D., Zhao, W., & Ross, A. R. (1998). Crustal structure of Himalaya orogeny at ~90 east longitude from INDEPTH deep reflection profiles. *Tectonics*, *17*(4), 481–500. https://doi.org/10.1029/98TC01314

He, R., Liu, G., Golos, E., Gao, R., & Zheng, H. (2014). Isostatic gravity anomaly, lithospheric scale density structure of the northern Tibetan plateau and geodynamic causes for potassic lava eruption in Neogene. *Tectonophysics*, *628*, 218–227. https://doi.org/10.1016/j.tecto.2014.04.047

He, R., Zhao, D., Gao, R., & Zheng, H. (2010). Tracing the Indian lithospheric mantle beneath central Tibetan plateau using teleseismic tomography. *Tectonophysics*, *491*(1–4), 230–243. https://doi.org/10.1016/j.tecto.2010.03.015

Henry, P., le Pichon, X., & Goffé, B. (1997). Kinematic, thermal and petrological model of the Himalayas: Constraints related to metamorphism within the underthrust Indian crust. *Tectonophysics*, *273*(1–2), 31–56. https://doi.org/10.1016/S0040-1951(96)00287-9

Hetényi, G., Cattin, R., Berthet, T., le Moigne, N., Chophel, J., Lechmann, S., et al. (2016). Segmentation of the Himalayas as revealed by arc-parallel gravity anomalies. *Scientific Reports*, *6*(1), 33866. https://doi.org/10.1038/srep33866

Hetényi, G., Cattin, R., Brunet, F., Bollinger, L., Vergne, J., Nabelek, J. L., & Diament, M. (2007). Density distribution of the India plate beneath the Tibetan plateau: Geophysical and petrological constraints on the kinetics of lower-crustal eclogitization. *Earth and Planetary Science Letters*, *264*(1–2), 226–244. https://doi.org/10.1016/j.epsl.2007.09.036

Hetényi, G., Cattin, R., Vergne, J., & Náblek, J. L. (2006). The effective elastic thickness of the India plate from receiver function imaging, gravity anomalies and thermomechanical modelling. *Geophysical Journal International*, *167*(3), 1106–1118. https://doi.org/10.1111/j.1365-246X.2006.03198.x

Hirn, A., Jiang, M., Sapin, M., Diaz, J., Nercessian, A., Lu, Q. T., et al. (1995). Seismic anisotropy as an indicator of mantle flow beneath the Himalayas and Tibet. *Nature*, *375*(6532), 571–574. https://doi.org/10.1038/375571a0

Holland, T. J. B., & Powell, R. (1998). An internally consistent thermodynamic data set for phases of petrological interest. *Journal of Metamorphic Geology*, *16*, 309–343.

Houseman, G., & England, P. (1993). Crustal thickening versus lateral expulsion in the Indian-Asian continental collision. *Journal of Geophysical Research*, *98*(B7), 12,233–12,249. https://doi.org/10.1029/93JB00443

Huang, W. C., Ni, J. F., Tilmann, F., Nelson, D., Guo, J., Zhao, W., et al. (2000). Seismic polarization anisotropy beneath the central Tibetan plateau. *Journal of Geophysical Research*, *105*(B12), 27,979–27,989. https://doi.org/10.1029/2000JB900339

Jiang, M., Galvé, A., Hirn, A., de Voogd, B., Laigle, M., Su, H. P., et al. (2006). Crustal thickening and variations in architecture from the Qaidam Basin to the Qang Tang (north-central Tibetan plateau) from wide-angle reflection seismology. *Tectonophysics*, *412*(3–4), 121–140. https://doi.org/10.1016/j.tecto.2005.09.011

Jiang, X., Jin, Y., & McNutt, M. K. (2004). Lithospheric deformation beneath the Altyn Tagh and West Kunlun faults from recent gravity surveys. *Journal of Geophysical Research*, *109*, B05406. https://doi.org/10.1029/2003JB002444

Jiménez-Munt, I., Fernandez, M., Verges, J., & Platt, J. P. (2008). Lithosphere structure underneath the Tibetan plateau inferred from elevation, gravity and geoid anomalies. *Earth and Planetary Science Letters*, *267*(1–2), 276–289. https://doi.org/10.1016/j.epsl.2007.11.045

Jiménez-Munt, I., & Platt, J. P. (2006). Influence of mantle dynamics on the topographic evolution of the Tibetan plateau: Results from numerical modeling. *Tectonics*, *25*, TC6002. https://doi.org/10.1029/2006TC001963

Jin, Y., McNutt, M. K., & Zhu, Y. (1994). Evidence from gravity and topography data for folding of Tibet. *Nature*, *371*(6499), 669–674. https://doi.org/10.1038/371669a0

Jin, Y., McNutt, M. K., & Zhu, Y. (1996). Mapping of descent of Indian and Eurasian plates beneath the Tibetan plateau from gravity anomalies. *Journal of Geophysical Research*, *101*(B5), 11,275–11,290. https://doi.org/10.1029/96JB00531

Johnson, M. R. W. (2002). Shortening budgets and the role of continental subduction during the India-Asia collision. *Earth Science Reviews*, *59*(1–4), 101–123. https://doi.org/10.1016/S0012-8252(02)00071-5

Jordan, T. A., & Watts, A. B. (2005). Gravity anomalies, flexure and the elastic thickness structure of the India-Eurasia collisional system. *Earth and Planetary Science Letters*, *236*(3–4), 732–750. https://doi.org/10.1016/j.epsl.2005.05.036

Karplus, M. S., Zhao, W., Klemperer, S. L., Wu, Z., Mechie, J., Shi, D., et al. (2011). Injection of Tibetan crust beneath the south Qaidam Basin: Evidence from INDEPTH IV wide-angle seismic data. *Journal of Geophysical Research*, *116*, B07301. https://doi.org/10.1029/2010JB007911

Kind, R., & Yuan, X. (2010). Seismic images of the biggest crash on earth. *Science*, *329*(5998), 1479–1480. https://doi.org/10.1126/science.1191620

Kind, R., Yuan, X., Saul, J., Nelson, D., Sobolev, S. V., Mechie, J., et al. (2002). Seismic images of crust and upper mantle beneath Tibet: Evidence of Eurasian plate subduction. *Science*, *298*(5596), 1219–1221. https://doi.org/10.1126/science.1078115

Kosarev, G., Kind, R., Sobolev, S. V., Yuan, X., Hanka, W., & Oreshin, S. (1999). Seismic evidence for a detached Indian lithospheric mantle. *Science*, *283*(5406), 1306–1309. https://doi.org/10.1126/science.283.5406.1306

Kumar, A., Fernàndez, M., Jiménez-Munt, I., Torne, M., Vergés, J., & Afonso, J. C. (2019). LitMod2D_2.0: An improved tool for the interpretation of upper mantle anomalies; *DIGITAL.CSIC*; http://doi.org/10.20350/digitalCSIC/9063

Kumar, A., Fernàndez, M., Jiménez-Munt, I., Torne, M., Vergés, J., & Afonso, J. C. (2020). LitMod2D_2.0: An improved integrated geophysical-petrological modeling tool for the physical interpretation of upper mantle anomalies. *Geochemistry, Geophysics, Geosystems*, *21*, e2019GC008777. https://doi.org/10.1029/2019GC008777

Kumar, P., Yuan, X., Kind, R., & Kosarev, G. (2005). The lithosphere-asthenosphere boundary in the Tien Shan-Karakoram region from S-receiver functions: Evidence from continental subduction. *Geophysical Research Letters*, *32*, L07305. https://doi.org/10.1029/2004GL022291

Kumar, P., Yuan, X., Kind, R., & Ni, J. (2006). Imaging the colliding Indian and Asian lithospheric plates beneath Tibet. *Journal of Geophysical Research*, *111*, B06308. https://doi.org/10.1029/2005JB003930

Le Pichon, X., Henry, P., & Goffé, B. (1997). Uplift of Tibet: From eclogites to granulites. *Tectonophysics*, *273*(1–2), 57–76. https://doi.org/10.1016/S0040-1951(96)00288-0

Lebedev, S., & van der Hilst, R. D. (2008). Global upper mantle tomography with the automated multimode inversion of surface and S-wave forms. *Geophysical Journal International*, *173*(2), 505–518. https://doi.org/10.1111/j.1365-246X.2008.03721.x

Leech, L. M. (2001). Arrested orogenic development: Eclogitization, delamination, and tectonic collapse. *Earth and Planetary Science Letters*, *185*(1–2), 149–159. https://doi.org/10.1016/S0012-821X(00)00374-5

Levin, V., Roecker, S., Graham, P., & Hosseini, A. (2008). Seismic anisotropy indicators in Western Tibet: Shear wave splitting and receiver function analysis. *Tectonophysics*, *462*, 99–108.

Li, C., van der Hist, R. D., Meltzer, A. S., & Robert Enghahi, E. (2008). Subduction of the Indian lithosphere beneath the Tibetan plateau and Burma. *Earth and Planetary Science Letters*, *274*(1–2), 157–168. https://doi.org/10.1016/j.epsl.2008.07.016

Li, J., & Song, X. (2018). Tearing of Indian mantle lithosphere from high resolution seismic images and its implications for lithosphere coupling in southern Tibet. *Proceedings of the National Academy of Sciences of the United States of America*, *115*(33), 8296–8300. https://doi.org/10.1073/pnas.1717258115

Li, S., Mooney, W. D., & Fan, J. (2006). Crustal structure of mainland China from deep seismic sounding data. *Tectonophysics*, *420*(1–2), 239–252. https://doi.org/10.1016/j.tecto.2006.01.026

Liang, X., Sandvol, E., Chen, Y. J., Hearn, T., Ni, J., Klemperer, S., et al. (2012). A complex Tibetan upper mantle: A fragmented Indian slab and no south-verging subduction of Eurasian lithosphere. *Earth and Planetary Science Letters*, *333–334*, 101–111.

Lowry, A. R., & Smith, R. B. (1994). Flexural rigidity of the basin and range–Colorado Plateau–Rocky Mountain transition from the coherence analysis of gravity and topography. *Journal of Geophysical Research*, *99*, 20,123–20,140.

Lyon-Caen, H., & Molnar, P. (1983). Constraints on the structure of the Himalaya from an analysis of gravity anomalies and a flexural model of the lithosphere. *Journal of Geophysical Research*, *88*(B10), 8171–8191. https://doi.org/10.1029/JB088iB10p08171

McKenzie, D., McKenzie, J., & Fairhead, D. (2019). The mechanical structure of Tibet. *Geophysical Journal International*, *217*(2), 950–969. https://doi.org/10.1093/gji/ggz052

McNamara, D. E., Owens, T. J., Silver, P. G., & Wu, F. T. (1994). Shear wave anisotropy beneath the Tibetan plateau. *Journal of Geophysical Research*, *99*(B7), 13,655–13,665. https://doi.org/10.1029/93JB03406

McNamara, D. E., Owens, T. J., & Walter, W. R. (1995). Observations of regional phase propagation across the Tibetan plateau. *Journal of Geophysical Research*, *100*(B11), 22,215–22,229. https://doi.org/10.1029/95JB01863

McNamara, D. E., Walter, W. R., Owens, T. J., & Ammon, C. J. (1997). Upper mantle velocity structure beneath the Tibetan plateau from Pn travel time tomography. *Journal of Geophysical Research*, *102*(B1), 493–505. https://doi.org/10.1029/96JB02112

Miller, C., Schuster, R., Klotzli, U., Frank, W., & Purtscheller, F. (1999). Post-collisional potassic and ultrapotassic magmatism in SW Tibet: Geochemical and Sr-Nd-Pb-O isotopic constraints for mantle source characteristics and petrogenesis. *Journal of Petrology*, *40*(9), 1399–1424. https://doi.org/10.1093/petroj/40.9.1399

Mishra, D. C., Ravi Kumar, M., & Arora, K. (2012). Long wavelength satellite gravity and geoid anomalies over Himalaya, and Tibet: Lithospheric structures and seismotectonics of intermediate focus earthquakes of Hindu Kush–Pamir and Burmese arc. *Journal of Asian Earth Sciences*, *48*, 93–110. https://doi.org/10.1016/j.jseaes.2011.12.003

Mitra, S., Priestley, K., Bhattacharyya, A. K., & Gaur, V. K. (2005). Crustal structure and earthquake focal depths beneath northeastern India and southern Tibet. *Geophysical Journal International*, *160*, 227–248.

Molnar, P., England, P., & Martinod, J. (1993). Mantle dynamics, uplift of the Tibetan plateau and the Indian monsoon. *Reviews of Geophysics*, *31*(4), 357–396. https://doi.org/10.1029/93RG02030

Monsalve, G., Sheehan, A., Rowe, C., & Rajaure, S. (2008). Seismic structure of the crust and the upper mantle beneath the Himalaya: Evidence for eclogitization of lower crustal rocks in the Indian Plate. *Journal of Geophysical Research*, *113*, B08315. https://doi.org/10.1029/2007JB005424

Murphy, M. A., Yin, A., Harrison, T. M., Dürr, S. B., Z, C., Ryerson, F. J., et al. (1997). Significant crustal shortening in southcentral Tibet prior to the Indo–Asian collision. *Geology*, *25*(8), 719–722. https://doi.org/10.1130/0091-7613(1997)025<0719:DTIACA>2.3.CO;2

Nabelek, J., Hetenyi, G., Vergne, J., Sapkota, S., Kafle, B., Jiang, M., et al. (2009). Underplating in the Himalaya-Tibet collision zone revealed by the Hi-CLIMB experiment. *Science*, *325*(5946), 1371–1374. https://doi.org/10.1126/science.1167719

Negredo, A. M., Replumez, A., Villasenor, A., & Guillot, S. (2007). Modeling the evolution of continental subduction process in the Pamir-Hindu Kush region. *Earth and Planetary Science Letters*, *259*(1–2), 212–225. https://doi.org/10.1016/j.epsl.2007.04.043

Nelson, K. D., Zhao, W., Brown, L. D., Kuo, J., Che, J., Liu, X., et al. (1996). Partially molten middle crust beneath southern Tibet: Synthesis of project INDEPTH results. *Science*, *274*(5293), 1684–1688. https://doi.org/10.1126/science.274.5293.1684

Oreshin, S., Kiselev, S., Vinnik, L., Prakasam, K. S., Rai, S. S., Makeyeva, L., & Savvin, Y. (2008). Crust and mantle beneath western Himalaya, Ladakh and western Tibet from integrated seismic data. *Earth and Planetary Science Letters*, *271*(1–4), 75–87. https://doi.org/10.1016/j.epsl.2008.03.048

Owens, T. J., & Zandt, G. (1997). Implications of crustal property variations for models of Tibetan plateau evolution. *Nature*, *387*(6628), 37–43. https://doi.org/10.1038/387037a0

Pan, Y., Shen, W.-B., Shum, C. K., & Chen, R. (2018). Spatially varying surface seasonal oscillations and 3-D crustal deformation of the Tibetan plateau derived from GPS and GRACE data. *Earth and Planetary Science Letters*, *502*, 12–22. https://doi.org/10.1016/j.epsl.2018.08.037

Pavlis, N. K., Holmes, S. A., Kenyon, S. C., & Factor, J. K. (2012). The development and evaluation of the earth gravitational model 2008 (EGM2008). *Journal of Geophysical Research*, *117*, B04406. https://doi.org/10.1029/2011JB008916

Priestley, K., Debayle, E., Mckenzie, D., & Pilidou, S. (2006). Upper mantle structure of eastern Asia from multimode surface waveform tomography. *Journal of Geophysical Research*, *111*, B10304. https://doi.org/10.1029/2005JB004082

Priestley, K., Ho, T., & Mitra, S. (2019). The crustal structure of the Himalaya: A synthesis. *Geological Society, London, Special Publications*, *483*(1), 483–516. https://doi.org/10.1144/SP483-2018-127

Priestley, K., Jackson, J., & McKenzie, D. (2008). Lithospheric structure and deep earthquakes beneath India, the Himalaya and southern Tibet. *Geophysical Journal International*, *172*(1), 345–362. https://doi.org/10.1111/j.1365-246X.2007.03636.x

Rai, S. S., Pristley, K., Gaur, V. K., Mitra, S., Sing, M. P., & Searle, M. (2006). Configuration of the Indian Moho beneath the NW Himalaya. *Geophysical Research Letters*, *33*, L15308. https://doi.org/10.1029/2006GL026076

Ramesh, D. S., Ravi Kumar, M., Uma Devi, E., & Raju, P. S. (2005). Moho geometry and upper mantle images of northeast India. *Geophysical Research Letters*, *32*, L14301. https://doi.org/10.1029/2005GL022789

Ravikumar, M., Mishra, D. C., & Singh, B. (2013). Lithosphere, crust and basement ridges across Ganga and Indus basins and seismicity along the Himalayan front, India and Western Fold Belt, Pakistan. *Journal of Asian Earth Science*, *75*, 126–140. https://doi.org/10.1016/j.jseaes.2013.07.004

Ravikumar, M., Mishra, D. C., Singh, B., Venkat Raju, D. C., & Singh, M. (2013). Geodynamics of NW India: Subduction, lithospheric flexure, ridges and seismicity. *Journal Geological Society of India*, *81*(1), 61–78. https://doi.org/10.1007/s12594-013-0006-x

Replumaz, A., Guillot, S., Villaseñor, A., & Negredo, A. M. (2013). Amount of Asian lithospheric mantle subducted during the India/Asia collision. *Gondwana Research*, *24*(3–4), 936–945. https://doi.org/10.1016/j.gr.2012.07.019

Replumaz, A., Negredo, A. M., Villaseñor, A., & Guillot, S. (2010). Indian continental subduction and slab break-off during tertiary collision. *Terra Nova*, *22*, 290–296.

Ries, J., Bettadpur, S., Eanes, R., Kang, Z., Ko, U. D., McCullough, C., et al. (2016). The combined gravity model GGM05C. *GFZ Data Services*. https://doi.org/10.5880/icgem.2016.002

Robert, A. M. M., Fernàndez, M., Jiménez-Munt, I., & Vergés, J. (2015). Lithospheric structures in Central Eurasia derived from elevation, geoid anomaly and thermal analysis. *Geological Society of London, Special Publication*, *427*. https://doi.org/10.1144/SP427.10

Sandvol, E., Ni, J., Kind, R., & Zhao, W. (1997). Seismic anisotropy beneath the southern Himalayas-Tibet collision zone. *Journal of Geophysical Research*, *102*(B8), 17,813–17,823. https://doi.org/10.1029/97JB01424

Schulte-Pelkum, V., Monsalve, G., Sheehan, A., Pandey, M. R., Sapkota, S., Bilham, R., & Wu, F. (2005). Imaging the Indian subcontinent beneath the Himalaya. *Nature*, *435*, 222–1225.

Searle, M. P. (2010). Geological Evolution of the Karakoram ranges, Italy. *Journal of Geoscience (Bollettino- Societa Geologica Italiana)*, *130*(2), 147–159. https://doi.org/10.3301/IJG.2011.08

Shapiro, N. M., & Ritzwoller, M. H. (2002). Monte-Carlo inversion for a global shear velocity model of the crust and upper mantle. *Geophysical Journal International*, *151*(1), 88–105. https://doi.org/10.1046/j.1365-246X.2002.01742.x

Shi, D., Wu, Z., Klemperer, S. L., Zhao, W., Xue, G., & Su, H. (2015). Receiver function imaging of crustal suture, steep subduction, and mantle wedge in the eastern India–Tibet continental collision zone. *Earth and Planetary Science Letters*, *414*, 6–15. https://doi.org/10.1016/j.epsl.2014.12.055

Shi, D., Zhao, W., Klemperer, S. L., Wu, Z., Mechie, J., Shi, J., et al. (2016). West-east transition from underplating to steep subduction in the India–Tibet collision zone revealed by receiver-function profiles. *Earth and Planetary Science Letters*, *452*, 171–177. https://doi.org/10.1016/j.epsl.2016.07.051

Shin, Y. H., Zu, H., Braitenberg, C., Fang, J., & Wang, Y. (2007). Moho undulations beneath Tibet from Grace integrated gravity data. *Geophysical Journal International*, *170*(3), 971–985. https://doi.org/10.1111/j.1365-246X.2007.03457.x

Silver, P. G., & Chan, W. W. (1991). Shear wave splitting and subcontinental mantle deformation. *Journal of Geophysical Research*, *96*(B10), 16,429–16,454. https://doi.org/10.1029/91JB00899

Simpson, R. W., Jachens, R. C., & Blakely, R. J. (1986). A new isostatic residual gravity map of the conterminous United States with a discussion on the significance of isostatic residual anomalies. *Journal of Geophysical Research*, *91*(B8), 8348–8372. https://doi.org/10.1029/JB091iB08p08348

Singh, A., Ravi Kumar, M., Mohanty, D. D., Singh, C., Biswas, R., & Srinagesh, D. (2017). Crustal structure beneath India and Tibet: New constraints from inversion of receiver functions. *Journal of Geophysical Research: Solid Earth*, *122*, 7839–7859. https://doi.org/10.1002/2017JB013946

Subba Rao, D. V. (1996). Resolving Bouguer anomalies in continents—A new approach. *Geophysical Research Letters*, *23*(24), 3543–3546. https://doi.org/10.1029/96GL03471

Talwani, M., Worzel, J., & Landisman, M. (1959). Rapid gravity computations for two dimensional bodies with application to the Mendocino submarine fracture zone. *Journal of Geophysical Research*, *64*(1), 49–59. https://doi.org/10.1029/JZ064i001p00049

Taylor, M., & Yin, A. (2009). Active structures of the Himalayan-Tibet orogen and their relationships to earthquake distribution, contemporary strain field, and Cenozoic volcanism. *Geosphere*, *5*(3), 199–214. https://doi.org/10.1130/GES00217.1

Tenzer, R., Chen, W., & Jin, S. (2015). Effect of upper mantle density structure on Moho geometry. *Pure and Applied Geophysics*, *172*(6), 1563–1583. https://doi.org/10.1007/s00024-014-0960-2

Tilmann, F., Ni, J., & INDEPTH III Seismic Team (2003). Seismic imaging of the downwelling Indian lithosphere beneath Central Tibet. *Science*, *300*(5624), 1424–1427. https://doi.org/10.1126/science.1082777

Tiwari, V. M., Rajasekhar, R. P., & Mishra, D. C. (2008). Gravity anomaly, lithospheric structure and seismicity of Western Himalayan Syntaxis. *Journal of Seismology*, *13*(3), 363–370. https://doi.org/10.1007/s10950-008-9102-6

Tiwari, V. M., Rao, M. B. S. V., Mishra, D. C., & Singh, B. (2006). Crustal structure across Sikkim, NE Himalaya from new gravity and magnetic data. *Earth and Planetary Science Letters*, *247*(1–2), 61–69. https://doi.org/10.1016/j.epsl.2006.03.037

Tiwari, V. M., Ravi Kumar, M., & Mishra, D. C. (2013). Long wavelength gravity anomalies over India: Crustal and lithospheric structures and its flexure. *Journal of Asian Earth Sciences*, *70–71*, 169–178.

Tseng, T. L., Chen, W. P., & Nowack, R. L. (2009). Northward thinning of Tibetan crust revealed by virtual seismic profiles. *Geophysical Research Letters*, *36*, L24304. https://doi.org/10.1029/2009GL040457

Tunini, L., Jiménez-Munt, I., Fernandez, M., Vergés, J., & Villaseñor, A. (2015). Lithospheric mantle heterogeneities beneath the Zagros Mountains and the Iranian plateau: A petrological-geophysical study. *Geophysical Journal International*, *200*(1), 596–1614. https://doi.org/10.1093/gji/ggu418

Tunini, L., Jiménez-Munt, I., Fernandez, M., Vergés, J., Villaseñor, A., Melchiorre, M., & Afonso, J. C. (2016). Geophysical-petrological model of the crust and upper mantle in the India-Eurasia collision zone. *Tectonics*, *35*, 1642–1669. https://doi.org/10.1002/2016TC004161

Turcotte, D. L., & Schubert, D. (2001). *Geodynamics* (Vol. 213, 2nd ed.). Cambridge: Cambridge University Press.

Turcotte, D. L., & Schubert, G. (1982). *Geodynamics: Applications of continuum physics to geological problems* (1st ed.). New York: John Wiley.

Turner, S., Arnaud, N., Liu, J., Rogers, N., Hawkesworth, C., Harris, N., et al. (1996). Post-collision, shoshonitic volcanism on the Tibetan plateau: Implications for convective thinning of the lithosphere and source of ocean island basalts. *Journal of Petrology*, *37*(1), 45–71. https://doi.org/10.1093/petrology/37.1.45

Unsworth, M., Wei, W., Jones, A. G., Li, S., Bedrosian, P., Booker, J., et al. (2004). Crustal and upper mantle structure of northern Tibet imaged with magnetotelluric data. *Journal of Geophysical Research*, *109*, B02403. https://doi.org/10.1029/2002JB002305

Unsworth, M. J., Jones, A. G., Wei, G., Gokarn, S. G., Spratt, J. E., & INDEPTH-MT team (2005). Crustal rheology of the Himalaya and southern Tibet inferred from magnetotelluric data. *Nature*, *438*(7064), 78–81. https://doi.org/10.1038/nature04154

Vening Meinesz, F. A. (1931). Une nouvelle methode pour la reduction isostatique regionale de l'intensite de la pesanteur. *Bulletine Geodesique*, *29*(1), 33–51. https://doi.org/10.1007/BF03030038

Wang, Q., Hawkesworth, C. J., Wyman, D., Chung, S. L., Wu, F. Y., Li, X. H., et al. (2016). Pliocene-quaternary crustal melting in central and northern Tibet and insights into crustal flow. *Nature Communications*, *7*(1), 11888. https://doi.org/10.1038/ncomms11888

Watts, A. B. (2001). *Isostasy and flexure of the lithosphere* (First ed.). Cambridge: Cambridge University Press.

Wei, W., Unsworth, M., Jones, A., Booker, J., Tan, H., Nelson, D., et al. (2001). Detection of widespread fluids in the Tibetan crust by magnetotelluric studies. *Science*, *292*(5517), 716–719. https://doi.org/10.1126/science.1010580

Wessel, P., & Smith, W. H. F. (1995). New version of the generic mapping tools. *Eos Transactions American Geophysical Union*, *76*, 329. https://doi.org/10.1029/95EO00198

Wittlinger, G., Farra, V., Hetényi, G., Vergne, J., & Nábělek, J. (2009). Seismic velocities in southern Tibet lower crust: A receiver function approach for eclogite detection. *Geophysical Journal International*, *177*, 1037–1049. https://doi.org/10.1111/j.1365-246X.2008.04084.x

Wittlinger, G., Vergne, J., Tapponnier, P., Farra, V., Poupinet, G., Jiang, M., et al. (2004). Teleseismic imaging of subducting lithosphere and Moho offsets beneath western Tibet. *Earth and Planetary Science Letters*, *221*(1–4), 117–130. https://doi.org/10.1016/S0012-821X(03)00723-4

Wu, J., Zhang, Z., Kong, F., Yang, B. B., Yu, Y., Liu, K. H., & Gao, S. S. (2015). Complex seismic anisotropy beneath western Tibet and its geodynamic implications. *Earth and Planetary Science Letters*, *413*, 167–175. https://doi.org/10.1016/j.epsl.2015.01.002

Xia, L., Ma, Z., Xu, X., & Xia, Z. (2011). Cenozoic volcanism and tectonic evolution of the Tibetan plateau. *Gondwana Research*, *19*(4), 850–866. https://doi.org/10.1016/j.gr.2010.09.005

Yin, A., & Harrison, T. M. (2000). Geologic evolution of the Himalayan–Tibetan orogen. *Annual Review of Earth and Planetary Sciences*, *28*(1), 211–280. https://doi.org/10.1146/annurev.earth.28.1.211

Yue, H., Chen, Y. J., Sandvol, E., Ni, J., Hearn, T., Zhou, S., et al. (2012). Lithospheric and upper mantle structure of the northeastern Tibetan plateau. *Journal of Geophysical Research*, *117*, B05307. https://doi.org/10.1029/2011JB008545

Zeyen, H., Ayarza, P., Fernandez, M., & Rimi, A. (2005). Lithospheric structure under the western African-European plate boundary: A transect across the Atlas Mountains and the Gulf of Cadiz. *Tectonics*, *24*, TC2001. https://doi.org/10.1029/2004TC001639

Zeyen, H., & Fernàndez, M. (1994). Integrated lithospheric modeling combining thermal, gravity, and local isostasy analysis: Application to the NE Spanish geotransect. *Journal of Geophysical Research*, *99*(B9), 18,089–18,102. https://doi.org/10.1029/94JB00898

Zhang, P. Z., Shen, Z., Wang, M., Gan, W., Bürgmann, R., Molnar, P., et al. (2004). Continuous deformation of the Tibetan plateau from global positioning system data. *Geological Society of America*, *32*(9), 809–812. https://doi.org/10.1130/G20554.1

Zhang, Z., Wang, Y., Houseman, G. A., Xu, T., Wu, Z., Yuan, X., et al. (2014). The Moho beneath western Tibet: Shear zones and eclogitization in the lower crust. *Earth and Planetary Science Letters*, *408*, 370–377, ISSN0012-821X. https://doi.org/10.1016/j.epsl.2014.10.022

Zhang, Z., Xiao, X., Wang, J., Wang, Y., & Kusky, T. M. (2008). Post-collisional Plio-Pleistocene shoshonitic volcanism in the western Kunlun Mountains, NW China: Geochemical constraints on mantle source characteristics and hetrogenesis. *Journal of Asian Earth Science*, *31*(4–6), 379–403. https://doi.org/10.1016/Journaljseaes.2007.06.003

Zhao, G., Liu, J., Chen, B., Kaban, M. K., & Zheng, X. (2020). Moho beneath Tibet based on a joint analysis of gravity and seismic data. *Geochemistry, Geophysics, Geosystems*, *21*, e2019GC008849. https://doi.org/10.1029/2019GC008849

Zhao, J., Yuan, X., Liu, H., Kumar, P., Pei, S., Kind, R., et al. (2010). The boundary between the Indian and Asian plates below Tibet. *Proceedings of the National Academy of Sciences*, *107*(25), 11,229–11,233. https://doi.org/10.1073/pnas.1001921107

Zhao, W., Kumar, P., Mechie, J., Kind, R., Meissner, R., Wu, Z., et al. (2011). Tibetan plate overriding the Asian plate in central and northern Tibet. *Nature Geoscience*, *4*(12), 870–873. https://doi.org/10.1038/ngeo1309

Zhao, W., Mechie, J., Brown, L. D., Guo, J., Haines, S., Hearn, T., et al. (2001). Crustal structure of central Tibet as derived from project INDEPTH wide-angle seismic data. *Geophysical Journal International*, *145*(2), 486–498. https://doi.org/10.1046/j.0956-540x.2001.01402.x

Zhao, Z., Nelson, K. D., & project INDEPTH team (1993). Deep seismic reflection evidence for continental under thrusting beneath Southern Tibet. *Nature*, *361*, 557–559.

Zhou, H., & Murphy, M. A. (2005). Tomographic evidence for wholesale underthrusting of India beneath the entire Tibetan plateau. *Journal of Asian Earth Science*, *25*(3), 445–457. https://doi.org/10.1016/j.jseaes.2004.04.007